Atomization of evaporating stable microemulsion droplets

Bal Krishan [1], Preetika Rastogi [2,*], D. Chaitanya Kumar Rao [3], Niket S. Kaisare [2], Madivala G. Basavaraj [2] and Saptarshi Basu [1,†]

[1] *Department of Mechanical Engineering, Indian Institute of Science, Bengaluru 560012, India*
[2] *Department of Chemical Engineering, Indian Institute of Technology, Madras 600 036, India*
[3] *Department of Aerospace Engineering, Indian Institute of Technology, Kanpur 208016, India*

(Received 27 November 2025; accepted 6 May 2026; published 26 May 2026)

We investigate the fragmentation dynamics of acoustically levitated microemulsion droplets subjected to laser irradiation. The influence of irradiation intensity and emulsion composition on bubble dynamics and subsequent breakup characteristics is investigated. Our findings demonstrate an inverse relationship between irradiation intensity and the onset of vapor bubble nucleation, which is consistent with theory. Depending on the composition and irradiation intensity, distinct regimes of bubble growth are revealed. The growth and collapse of these bubbles result in droplet fragmentation via ligament-mediated breakup and sheet breakup. These breakup modes are governed by interfacial instabilities, including Faraday, Rayleigh-Taylor, and Plateau-Rayleigh mechanisms. The bubble growth and collapse events are quantified using a breakup impact parameter (β), which, in turn, reveals the onset of instability triggering droplet breakup. Consequently, the variations in ligament dynamics [using Weber number (We)] are explained and correlated to the respective bubble growth and collapse events. In particular, our experimental data show that small-sized bubbles (lower value of β) typically result in the ejection of high-momentum ligaments (larger We). Finally, we report the growth and collapse dynamics of a highly viscous bubble that forms toward the end of the droplet lifetime due to the high concentration of nonvolatile surfactant.

DOI: 10.1103/prbb-cbyr

I. INTRODUCTION

The evaporation and breakup of liquid droplets is an ubiquitous phenomenon, central to processes ranging from cloud formation and rainfall to spray drying [1,2], fuel combustion [3–6], and advanced manufacturing [7,8]. Atomization, in particular, refers to the process of transforming a liquid into a fine spray or mist. Efficient atomization of liquid fuels is fundamental to modern combustion systems, as it governs the droplet size distribution, evaporation rate, and mixing uniformity. These parameters directly influence combustion stability and the formation of pollutants. Understanding the mechanisms governing droplet breakup and atomization is essential for optimizing these processes and improving the efficiency of such systems [9–12].

The breakup of droplets is typically driven by the competition between disruptive forces, such as aerodynamic drag, shear stress, and turbulence, and stabilizing forces, such as surface tension and viscosity [9,13]. When the disruptive forces overcome the cohesive forces, the droplet deforms and eventually fragments into smaller droplets. Fragmentation can be achieved through various

[*] Present address: Material Sciences Division and The Molecular Foundry, Lawrence Berkeley National Laboratory, Berkeley, California 94720, USA.
[†] Contact author: sbasu@iisc.ac.in

mechanisms, for example, liquid droplet [14,15] or jet [16–18] in a cross flow, shock-induced drop breakup [12,19,20], and via impingement on solid and liquid surfaces. There are many instances where atomization is achieved via bubble breakup. For example, bursting bubbles at free liquid surfaces generate high-speed Worthington jets and daughter droplets, which play an important role in sea-spray aerosol production and interfacial mass transfer [21,22]. Bubble-induced fragmentation has also been reported in superheated and multicomponent droplets, where internal vapor bubble growth leads to microexplosion and secondary atomization [10,23]. Bubble-induced droplet disruption and jet-mediated secondary atomization have also been reported in reactive molten droplets, where internally generated gas cavities undergo repeated bursting and fragmentation cascades, as demonstrated by Inoue *et al.* [24] through the self-sustained breakup of reacting droplets driven by gas nucleation in molten fireworks. Atomization often involves the generation of a liquid jet or sheet that destabilizes and disintegrates into a cloud of fine droplets [13,25]. This process is influenced by parameters such as nozzle geometry, liquid properties, and the surrounding gas flow. For instance, in pressure-swirl atomizers, the liquid is forced through a small orifice, creating a thin sheet that breaks up due to Rayleigh-Taylor (RT) or Kelvin-Helmholtz (KH) instabilities [26].

Multicomponent liquids such as emulsion fuels have gained significant attention as potential alternative fuels for combustion applications, driven by their ability to enhance engine efficiency and mitigate harmful emissions (NO_x) [23,27]. Multiphase, multicomponent systems such as emulsions, nanofuels, and polymeric droplets are recognized for their practical significance and cross-disciplinary relevance [6,10,28–30]. Therefore, a comprehensive understanding of their spray and combustion behavior necessitates studying their breakup characteristics at a fundamental level. In particular, the addition of water to fuels in a water-in-oil emulsion lowers the overall combustion temperature, leading to a significant reduction in harmful particulate matter and gases [2,23,31]. In water-in-oil emulsions (i.e., macroemulsions), the significant volatility differential between the continuous (oil) and dispersed (water) phases allows the droplet to be heated beyond water's boiling temperature. This results in the superheating of the water subdroplets, leading to the formation of a vapor bubble. The subsequent expansion of this bubble consequently fragments the parent droplet [23,32]. As a result, heating the emulsion droplets results in bubble-induced breakup of the parent droplet, which can significantly enhance the atomization characteristics in spray systems. It has been reported that the fragmentation of distinct multicomponent droplets upon heating is primarily governed by the nucleation, growth, and subsequent rupture of internal bubbles [3,4,10,23,28,29,33,34].

Rao *et al.* [5,6] examined the complete sequence of events in a burning single droplet of a multicomponent fuel, identifying distinct bubble growth regimes and atomization mechanisms, and quantified how the change in droplet topology occurs. They demonstrated that internal bubble behavior critically controls the droplet breakup characteristics. Shinjo *et al.* [35] showed that the bubble growth and breakup dynamics are strongly influenced by both the size and location of the internal water subdroplets. It has been reported that smaller subdroplets, for instance, lead to only limited fragmentation of the parent droplet. Conversely, a higher degree of breakup is achieved when multiple nucleation events occur and interact simultaneously. Furthermore, it has been established that the evaporation and combustion characteristics of emulsions can be controlled by varying the composition of their constituents (oil, water, and surfactant) [2,23,34,36]. It was also shown that the addition of water enhances the strength of the droplet breakup [37,38].

The evaporation of acoustically levitated water-in-oil emulsion droplets under laser heating results in three distinct breakup modes [23]. The dominant breakup mechanisms are (1) bubble-growth-driven rupture with surface wave dynamics resembling Faraday instabilities (notable in water/decane), (2) sheet breakup from small, indiscernible bubbles producing crown rims and ligament pinch-off (more likely in water/dodecane), and (3) catastrophic breakup with prompt fine fragmentation when volatility differences are largest (water/tetradecane). A recent study by Priyadarshini *et al.* [3], on the combustion of stable water-in-oil microemulsion droplets, showed concurrent bubble growth, surface-bubble collapse, and the resulting capillary wave-driven breakup mechanisms. The authors also introduced a nondimensional bubble breakup impact parameter β that increases with dispersed-phase volume fraction ϕ. The detailed characterization of ligament

TABLE I. Properties of pure liquids used to prepare the microemulsions are presented (at 25 °C). Listed are the surface tension (σ), dynamic viscosity (μ), latent heat of vaporization ($\Delta_v H$), boiling point temperature (T), vapor pressure (p_v), density (ρ), c_p is the specific heat capacity, k thermal conductivity and absorption coefficient (α) for infrared electromagnetic waves of wavelength, $\lambda = 10.6$ μm.

Properties	Water	Decane	Dodecane	*p*-Xylene
σ (mN/m)	72.75	23.83	25.35	28.9
μ (mPa s)	0.89	0.85	1.36	0.58
$\Delta_v H$ (kJ/mol)	44	51.5	61.4	42.4
T(°C)	100	174	216	140
p_v (kPa)	2.3	0.19	0.018	1.16
ρ (kg/m^3)	997	730	750	860
c_p (kJ/kg K)	4.20	2.21	2.20	1.71
k (W/m K)	0.6	0.13	0.138	0.128
$\alpha\|_{\lambda=10.6\,\mu m}$ (m^{-1})	$O(10^5)$			

properties, such as aspect ratio and thickness, provides a direct link to the microemulsion properties and the breakup impact parameter β. In addition, it was found that the size of the ejected droplets increases with ligament diameter and decreases with ligament ejection velocity [9,13,22,39].

Most prior studies have investigated macroemulsions that are prone to phase separation and lack long-term stability. In addition, there is limited literature on the evaporation and atomization of stable emulsions [2,3,34]. This study examines the bubble-mediated breakup of stable microemulsion droplets under controlled laser heating. The current work presents a unique investigation into the dynamics of various bubble breakup modes. We report three distinct droplet fragmentation mechanisms (*Types A*, *B*, and *C*) that constitute different regimes, each strongly dependent on the heating rate and composition of the emulsions. In addition, five distinct bubble breakup modes are identified, which are dictated by different instability mechanisms, such as Faraday, Rayleigh-Taylor, and Plateau-Rayleigh instabilities, that dictate the fragmentation characteristics of the droplet. Finally, we observe a mode characterized by the repetitive growth and collapse of a highly viscous bubble. This behavior directly results from an increase in surfactant concentration, which significantly alters the emulsion composition and properties.

II. MATERIALS AND METHODOLOGY

Water-in-oil microemulsions were prepared using water as the dispersed phase and decane, dodecane, *p*-xylene, and surrogate (defined as the mixture of dodecane and *p*-xylene in the ratio 9:1 by mass) as the continuous oil phase (i.e., base oil). The properties of the pure components are tabulated in Table I. A double-tailed ionic surfactant, sodium bis(2-ethylhexyl) sulfosuccinate, commonly referred to as AOT or Aerosol-OT (±97%purity), was used to stabilize the microemulsions. All the chemicals were procured from Merck and used without any further modification. High-purity, freshly deionized water (resistivity, 18.2 MΩ-cm) obtained from a laboratory Milli-Q system (ELGA, Purelab Option-Q, DV 25) was used to prepare the samples.

A. Preparation and characteristics of microemulsions

Water-in-oil microemulsions consist of a thermodynamically stable dispersion of nanometer-sized water subdroplets stabilized by a monolayer of surfactant. These microemulsions are characterized by two compositional parameters: (1) molar ratio of water to AOT (i.e., ω) and (2) dispersed phase volume fraction (i.e., ϕ). The parameters ω and ϕ are defined as

$$\omega = \frac{[H_2O]}{[AOT]}, \quad \text{and} \quad \phi = \frac{V_{H_2O} + V_{AOT}}{V_{H_2O} + V_{AOT} + V_{oil}}, \tag{1}$$

TABLE II. Properties of microemulsions formulated with different base oils used in this study are listed here. All microemulsions correspond to $\omega = 10$ and $\phi = 0.4$ (see main text).

Properties	Decane	Dodecane	*p*-Xylene	Surrogate
ρ (kg/m^3)	918	885	964	889
μ (mPa.s)	32.35	36.84	6.39	28.80
σ (mN/m)	23.81	22.90	25.71	24.35

where [H_2O] and [AOT] denote the number of moles of water and AOT, respectively, and V denotes the volume of different components. As evident from Eq. (1), an increase in the concentration of water denotes an increase in ω and ϕ, and is typically used as a handle to tune the size and the number density of the dispersed water subdroplets [40], respectively.

For a given value of ω and ϕ, the corresponding mass of the continuous oil phase and AOT in the water-in-oil microemulsions can be calculated using Eq. (1) by providing the mass of water as an additional input variable. A predetermined quantity of AOT is precisely weighed and transferred into precleaned glass vials to prepare the microemulsion samples. Subsequently, an appropriate amount of the oil is added to the vials. The mixture is then shaken gently for a few minutes (depending on the relative quantity of AOT and oil) until the AOT is completely dissolved in the oil phase. Later, a weighed amount of deionized water is added to the oil-AOT mixture and shaken gently until the resulting sample becomes a single-phase optically clear fluid. The samples were stored for 3–4 h at room temperature (25 °C) to ensure equilibration and homogeneity before any experiments or characterization.

When a droplet is subjected to an acoustic field, sufficiently strong excitation can induce large deformations and eventual fragmentation, as demonstrated in previous studies [41–44]. The onset of such breakup depends on the acoustic field strength, droplet size, and thermophysical properties, particularly surface tension and viscosity. Heating reduces these stabilizing properties, thereby increasing susceptibility to acoustically driven instabilities. Microemulsions with lower ϕ and ω values are prone to such instabilities particularly at elevated heating rates.

In our previous work [2], conducted under relatively lower heating rates, we explored a broad range of parameters, with $\phi = 0.1$–0.4 and $\omega = 5$–40. Under these conditions, the emulsion droplet remained stable and no acoustically driven breakup was observed. In the present study, the primary objective is to isolate and investigate nucleation-induced droplet breakup. Accordingly, ω and ϕ are selected to suppress acoustically driven instabilities and ensure controlled, repeatable behavior. Based on these considerations, microemulsions were prepared with a fixed water-to -surfactant molar ratio of $\omega = 10$ and a dispersed phase volume fraction of $\phi = 0.4$, which lie within the stable regime identified in our prior work. Moreover, higher values of ϕ are associated with an increased likelihood of nucleation in the microemulsion as reported previously [34]. Accordingly, ϕ and ω were chosen such that the evaporation of emulsion droplet leads to increased nucleation activity and thus the breakup behavior.

The nanostructural details of the water-in-oil microemulsions at this composition can be found in our previous work [2]. The viscosity of the sample was measured using Anton Paar 302, equipped with a cone and plate tool. All the samples exhibited constant viscosity in the range of shear rate 0.01 to 1000. The results of rheological characterization are presented in the Supplemental Material [45] (see Fig. S1). The interfacial tension (σ) between the microemulsion and air was measured using the pendant drop method on an Attension Theta goniometer (Biolin Scientific), with a 14-gauge metal-hub Hamilton needle. The density of the microemulsions was determined using an Anton Paar DMA 4500M densitometer, with a 2 ml sample used for each measurement. All the properties of microemulsions are tabulated in the Table II.

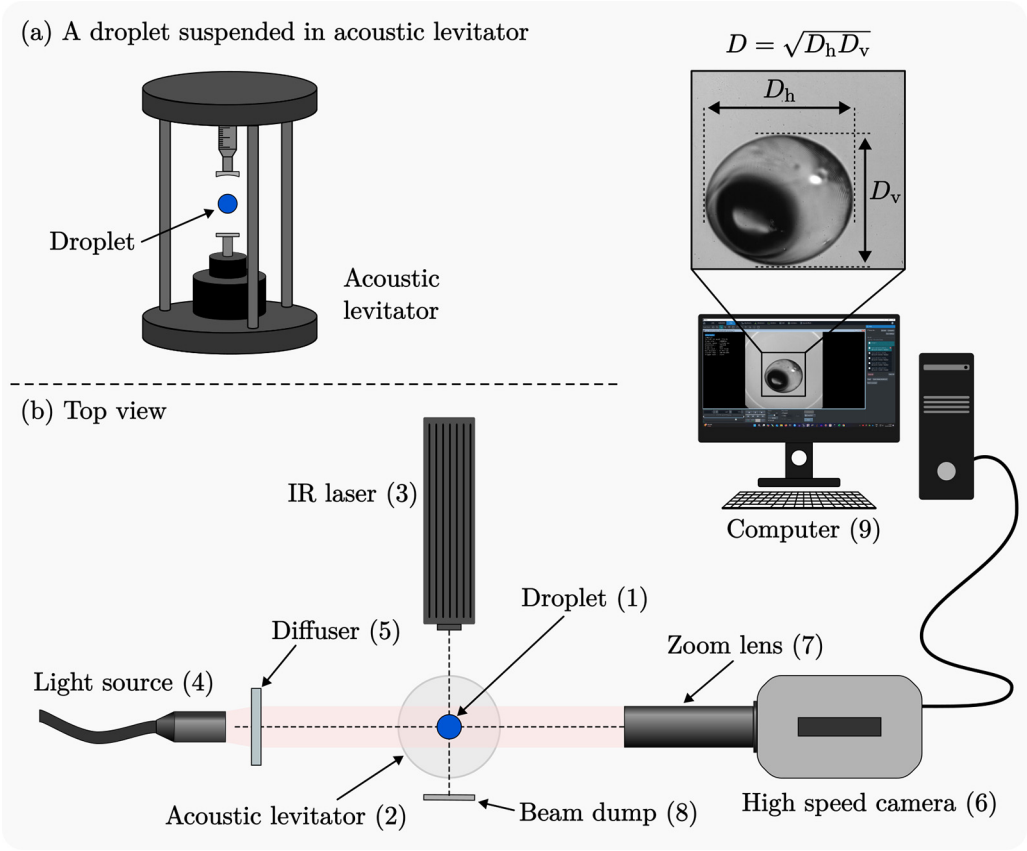

FIG. 1. (a) A droplet levitated using an acoustic levitator. (b) The top view of the experimental setup is shown, illustrating, a droplet (1) levitated using an acoustic levitator (2) and heated using an infrared laser (3). A laser light source (4) is used to project a shadow of the droplet onto the sensor of a high-speed camera (6) through a zoom lens (7), capturing magnified shadowgraphy images. A beam dump (8) was employed to intercept the infrared laser beam, ensuring safety. The recorded data was stored in the computer (9) for further processing.

B. Experimental details and postprocessing

The schematic of the experimental setup is shown in Fig. 1. A droplet of diameter $D_0 \sim 850 \pm 50$ μm is suspended using a single-axis acoustic levitator (Tec5) with a frequency of 100 kHz at standard ambient conditions. The droplet is heated externally at irradiation intensities $I^* = 0.1, 0.2, 0.4$, and 0.8, where $I^* = I/I_{max}$ and $I_{max} = 1.04\ \mathrm{MW/m^2}$ with a 3.5 mm beam diameter continuous CO_2 infrared (IR) laser (Synrad 48, wavelength $\lambda \sim 10.6$ μm, and maximum power ($P_{max} = 10$W). Droplet evaporation dynamics are recorded using a high-speed camera (Photron SA5) with a high-speed laser light source (CAVILUX$^{\#}$ Smart UHS, 640 nm).

A recording rate of 10 000 frames per second (fps) has been used, along with the spatial resolution of 5.2 μm per pixel. The droplet images are analyzed and processed using Photron's proprietary software PFV4 (x64) and ImageJ (version 1.53t). Python 3.11 and Inkscape 1.1.2 have been used for data plotting and figure preparation, respectively. The equivalent diameter of the droplet is calculated as $D_{eq} = \sqrt{D_h D_v}$, where D_h and D_v represent the maximum horizontal and vertical length scales (i.e., diameter) of the droplet as shown in Fig. 1.

III. RESULTS

A. Global overview

Upon laser activation, the microemulsion droplet absorbs the electromagnetic energy, resulting in internal heating of the droplet and an increase in its temperature. The absorption of energy depends on the irradiation parameters such as intensity (I) and wavelength (λ). Furthermore, the absorption characteristics of the droplet (α_λ) and initial size (D_0) significantly influence its thermophysical response [33,46]. Consequently, the optohydrodynamic response of the droplet, including evaporation, bubble nucleation, and eventual breakup is governed by the interplay between irradiation conditions and the properties of the microemulsions. At low irradiation intensities ($I^* \leqslant 0.1$), the microemulsion droplet predominantly exhibits undisruptive evaporation, as illustrated in Fig. 2(a). Under these conditions, the diameter of the droplet decreases steadily, primarily due to the vaporization of the volatile components. As evaporation proceeds, the nonvolatile constituents gradually accumulate at the droplet interface, eventually forming a shell. This shell acts as a barrier, significantly reducing the evaporation rate by inhibiting further mass transfer. Such shell formation is characteristic of multicomponent droplets containing nonvolatile species, and it plays a crucial role in modulating the late-stage evaporation dynamics (i.e., unsteady evaporation). A comprehensive analysis of the evaporation behavior of microemulsion droplets has been presented in our previous work [2].

With increasing irradiation intensity ($I^* > 0.1$), the droplet response transitions to evaporation with internal bubble nucleation. The higher energy uptake leads to localized superheating inside the droplet, triggering bubble nucleation at heterogeneous sites created by detached, nonvolatile surfactant. This process creates several microbubbles, which combine to form one or more large bubbles [3]. These bubbles then grow and eventually rupture, leading to fragmentation of the parent droplet and formation of fine secondary droplets. This transition between evaporation and nucleation regimes is reflected in the droplet regression curve, where bubble growth and rupture produce a distinct peak, as shown in Fig. 2(b). A schematic representation of these pathways is also shown in Fig. 2(c), which shows that, for $I^* \leqslant 0.1$, the droplet dynamics is purely driven by evaporation. In contrast, for $I^* \geqslant 0.1$, the dynamics are dominated by the bubble nucleation and breakup.

The laser-induced breakup of a microemulsion droplet is primarily governed by the irradiation intensity (I^*) and the thermophysical properties of the droplet. As reported by Krishan *et al.* [2], the microemulsion droplet undergoes three different stages of evaporation. Bubble nucleation primarily occurs during the steady evaporation (*stage II*) phase, except at a higher irradiation intensity ($I^* = 0.8$) where we observe nucleation during the preheating (*stage I*) phase.

At low irradiation intensity ($I^* = 0.1$), all microemulsion droplets exhibit undisruptive evaporation, except the xylene-based system, which shows vapor bubble nucleation. As the irradiation intensity increases ($I^* \geqslant 0.1$), bubble nucleation occurs in all microemulsions, leading to breakup of the parent droplet. The droplet undergoes successive stages of single or multiple bubble nucleation, growth, and rupture, ultimately disintegrating into fine secondary droplets. An overview of the droplet–laser interaction at various intensities is presented in Fig. 3 for microemulsions with different base oils. Three distinct breakup mechanisms (*Type A*, *Type B*, and *Type C*) have been identified, each strongly influenced by the laser intensity and the properties of the base oil. Type A typically occurs at lower irradiation intensities and is represented by the magenta color in Fig. 3, whereas Types B and C occur at higher irradiation intensities and are shown in green and orange, respectively. Cases of undisruptive evaporation are indicated in blue and are typically observed at $I^* \leqslant 0.1$ for all base oils except xylene. For breakup cases, the temporal image sequences in Fig. 3 correspond only to the initial stages of bubble growth and rupture at the onset of nucleation and do not represent the complete breakup dynamics. The onset time for bubble nucleation (t_{onset}) decreases with increasing irradiation intensity, while the intensity of breakup correspondingly increases. A detailed discussion of the different droplet breakup types is presented in the following section.

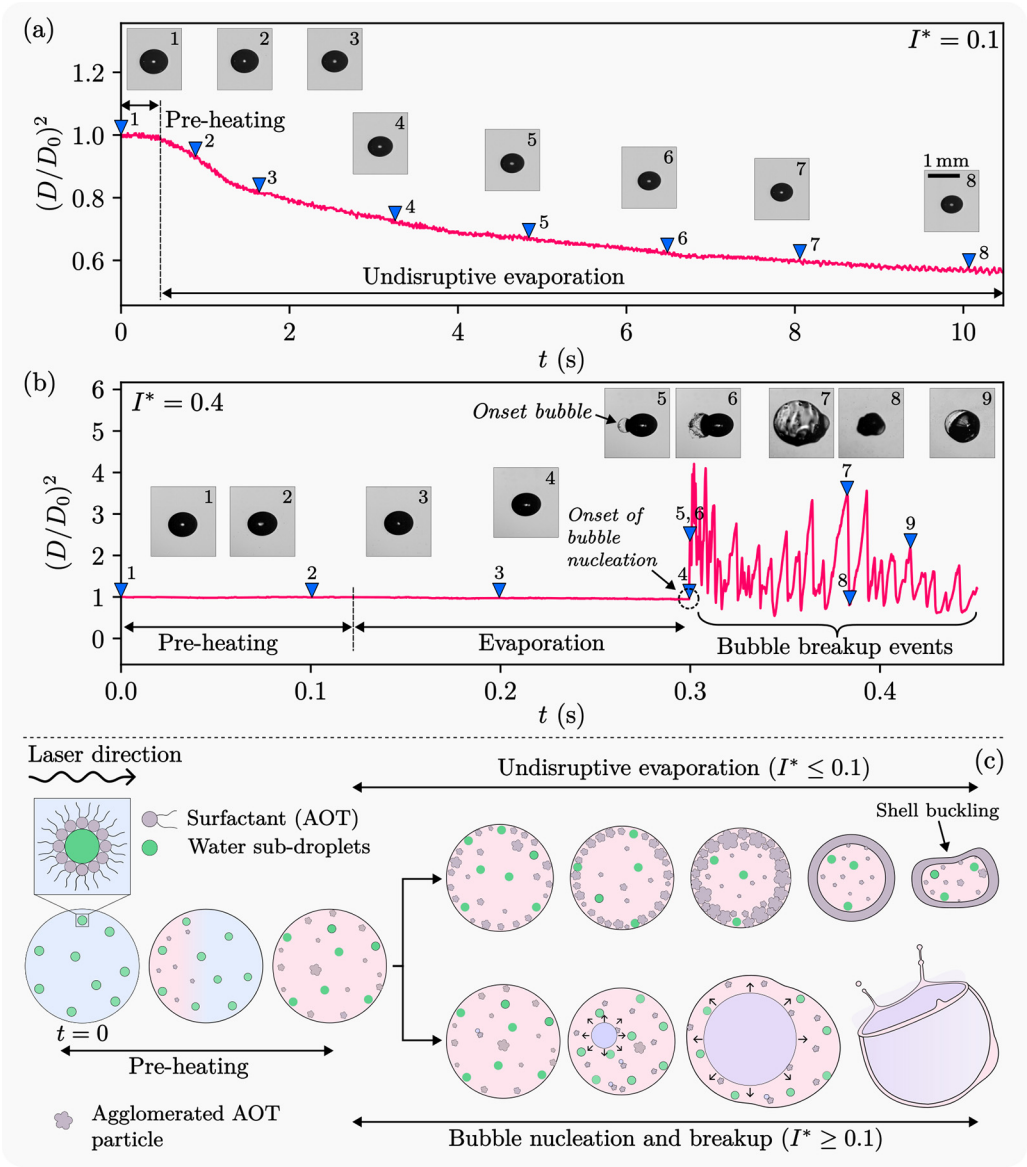

FIG. 2. Temporal evolution of the droplet diameter for a water-in-decane microemulsion ($\omega = 10$ and $\phi = 0.4$) droplet interacting with an IR laser. (a) Undisruptive evaporation at a low irradiation intensity of $I^* = 0.1$. (b) Evaporation accompanied by internal bubble nucleation at a higher irradiation intensity of $I^* = 0.4$, where each peak corresponds to a distinct bubble-induced breakup event. (c) A schematic of two distinct pathways for microemulsion droplet–laser interaction are shown, based on the irradiation intensity.

It is important to note that, as the droplet undergoes fragmentation, mass loss due to vaporization of the volatile component progressively increases the relative concentration of the nonvolatile surfactant (AOT). This compositional change significantly alters the liquid properties, including interfacial tension, viscosity, and internal phase distribution. In the present study, droplet breakup is initiated by bubble rupture, and each breakup event is accompanied by hydrodynamic instabilities (such as Rayleigh-Taylor destabilization) whose growth characteristics are strongly influenced by

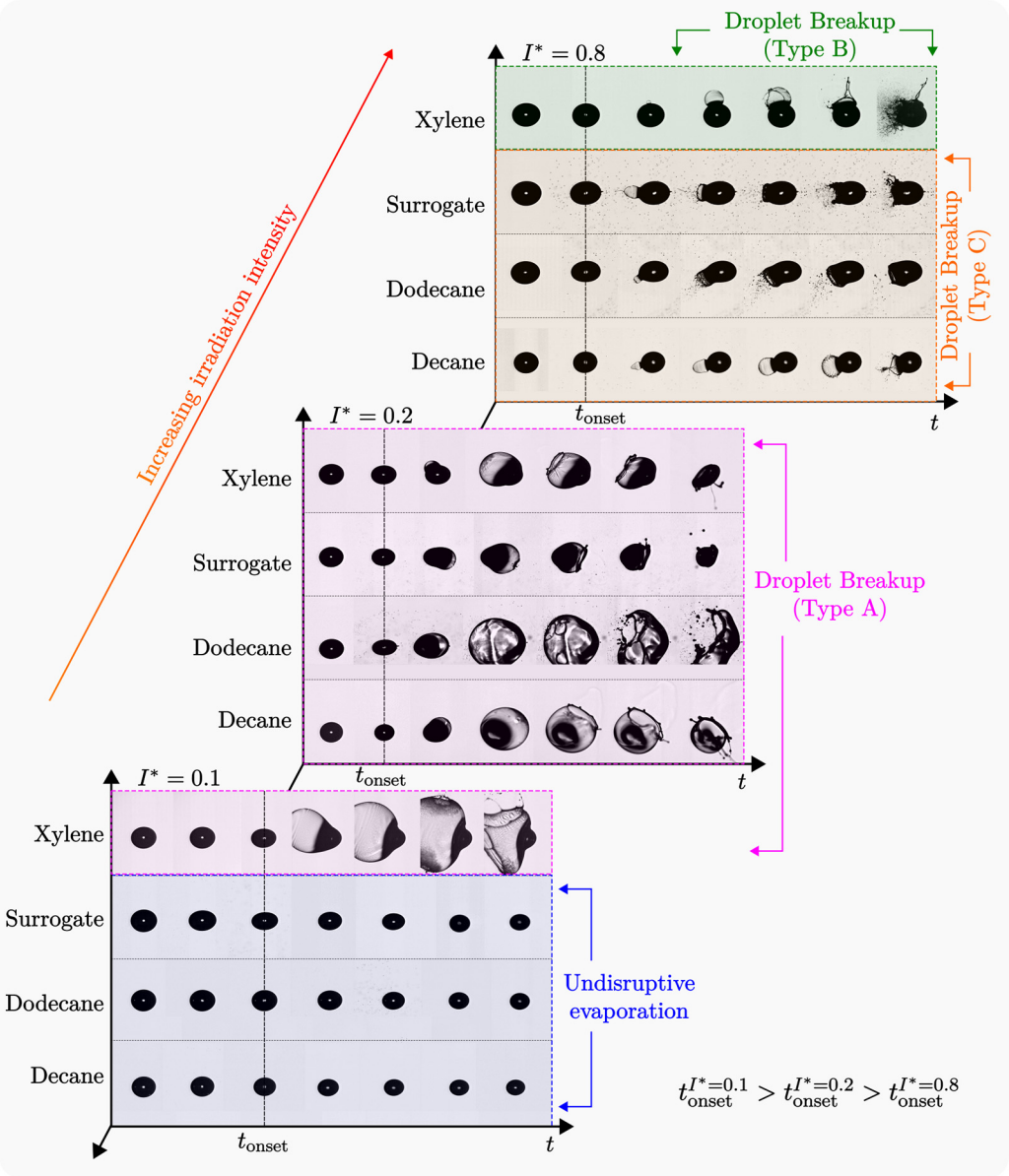

FIG. 3. Overview of the interaction between laser irradiation and a microemulsion droplet, showing time-series images for different base oils at three irradiation intensities. At $I^* = 0.1$, all base oils except xylene exhibit stable, undisruptive evaporation (indicated in blue), whereas higher irradiation intensities lead to distinct breakup mechanisms, namely *Type A*, *Type B*, and *Type C*, marked in magenta, green, and orange, respectively. The image sequences are shown only up to the nucleation and rupture of the first (onset) bubble. A longer onset time is observed under lower irradiation intensity.

the evolving droplet properties. These effects are reflected in the breakup dynamics observed across different regimes, as discussed later.

B. Mechanisms of droplet breakup

Three distinct mechanisms of droplet breakup have been identified, which are referred to as *Type A*, *Type B*, and *Type C*, based on the onset of bubble nucleation and subsequent droplet breakup behavior. Each breakup type undergoes various stages of bubble growth and rupture, which are referred to as *Regimes*. Each droplet breakup mechanism (i.e., *Type*) consists of multiple *Regimes*, which are governed by distinct bubble growth and bursting/rupture mechanisms. It is important to clarify that the regime numbering (I–V) is specific to each breakup Type and reflects the chronological sequence within that particular mechanism. Regime I in Type A is not physically identical to Regime I in Types B or C (where similarities exist, they are explicitly stated). The classification of these regimes is based on the temporal evolution and rupture dynamics of nucleated bubbles, along with the underlying hydrodynamic instabilities that govern the breakup behavior. In general, each regime is characterized by a distinct bubble breakup mode that ultimately leads to droplet disintegration.

Before discussing the bubble nucleation and breakup mechanisms, it is important to mention the stochasticity associated with the experiments, as the nucleation process is inherently stochastic in nature [47–49]. To ensure the repeatability, experiments were repeated multiple times, with a minimum of eight repetitions for each set of operating conditions for each sample. While some variability is observed in the exact timing of nucleation, bubble growth rate, and rupture, the overall breakup mode and regime classification are highly reproducible. Out of the total number of trials performed under identical operating conditions, the reported breakup dynamics were consistently observed in more than 85% of the trials, indicating a high degree of repeatability of the temporally evolving breakup regimes, despite the inherently stochastic nature of the nucleation process.

It should be noted that all presented data (images and plots) showing the temporal evolution of the droplet correspond to a representative single trial selected to illustrate the dominant breakup dynamics, unless stated otherwise. The images, in particular, are intended to provide a clear visual representation of the observed phenomena.

For *Type A* breakup, five distinct regimes governed by bubble rupture dynamics have been observed, as shown in Fig. 4. These regimes are unique to Type A and describe the sequential evolution of nucleated vapor bubbles under relatively low irradiation conditions. *Regime I* corresponds to the growth and rupture of a single vapor bubble formed at the onset of nucleation. In this regime, a single bubble emerges within the droplet and expands to a size typically exceeding the initial droplet diameter ($D_{b,\max}/D_0 > 1$). Subsequently, capillary waves are observed to develop on the bubble surface, and their amplification leads to rupture, ejecting vapor and generating ligaments along the receding rim. These ligaments fragment into small secondary droplets. Following this initial rupture, direct laser exposure of the droplet core initiates multiple nucleations, leading to the simultaneous growth of multiple bubbles. These bubbles subsequently rupture, producing fine secondary droplets. This stage is defined as *Regime II*. This highly transient process ($t \sim O(10^{-1})$) produces a large number of secondary droplets and substantial vapor ejection, resulting in significant mass loss and compositional variation.

Regime III is characterized by the coalescence of multiple bubbles into a single larger bubble, which subsequently collapses. The experimental sequence illustrating the merging of two bubbles into a single, larger bubble is shown in Fig. 4 (*Regime III*). Notably, this merging does not produce secondary droplets. However, the collapsing bubble may eject a liquid ligament from within. This ejected ligament can further disintegrate into fine secondary droplets. Such ligament ejection and breakup events are referred to as *Regime IV*. A visual representation of *Regime IV* is shown in Fig. 4 ($\Delta t = 75.2$–79 ms), for the nonbreakup case.

Finally, the droplet undergoes single-bubble growth and collapse (*Regime V*), where a bubble forms, expands, and subsequently collapses. This is the later stage, where the droplet properties differ significantly due to mass loss throughout all preceding regimes. As time progresses, reaching the onset of *Regime V*, substantial mass loss of the volatile components occurs, and the properties of the remaining fluid change significantly. This results in a transition from a less viscous liquid to

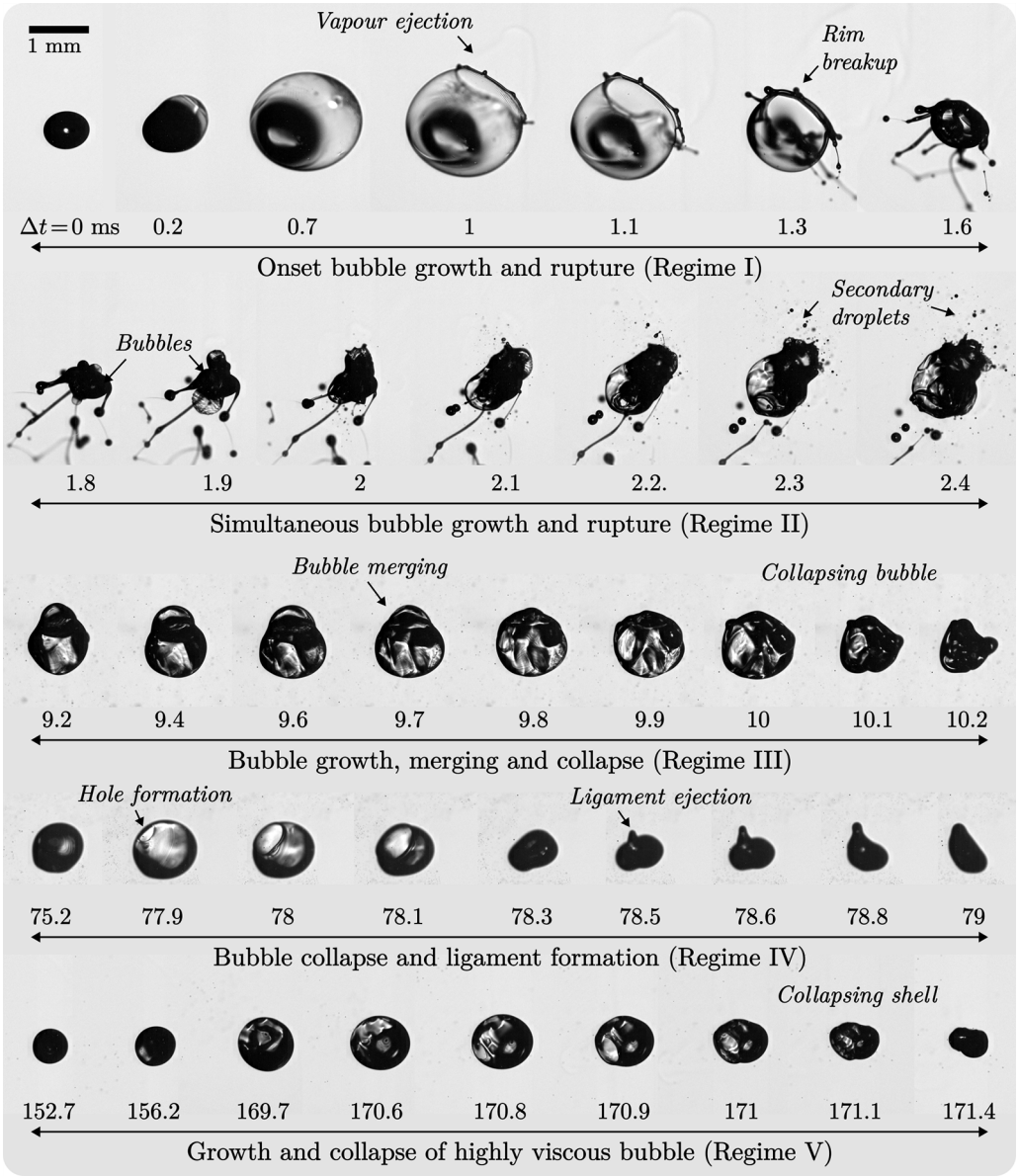

FIG. 4. *Breakup Type A*: Sequence of images illustrating the five distinct regimes observed during *Type A* breakup of a decane microemulsion at $I^* = 0.2$. The timescale (Δt) is referenced to the bubble nucleation onset (t_{onset}), such that $\Delta t = t - t_{\text{onset}}$. A complete video of the process is provided in the Supplemental Material [45] (see Video V1).

a highly viscous state, where the growth rate of the bubble is drastically reduced. Consequently, the final regime is characterized by the growth and collapse of this highly viscous bubble. It is noteworthy that *Regimes III*, *IV*, and *V* evolve more slowly than *Regimes I* and *II*, primarily due to the higher concentration of the nonvolatile surfactant (AOT), which increases the droplet viscosity. Collectively, these five regimes of bubble growth, rupture, and collapse cycles constitute the complete droplet breakup process. However, *Regimes III* and *V* typically do not contribute to atomization due to the variation in instantaneous properties. In fact, *Regime V* can be considered

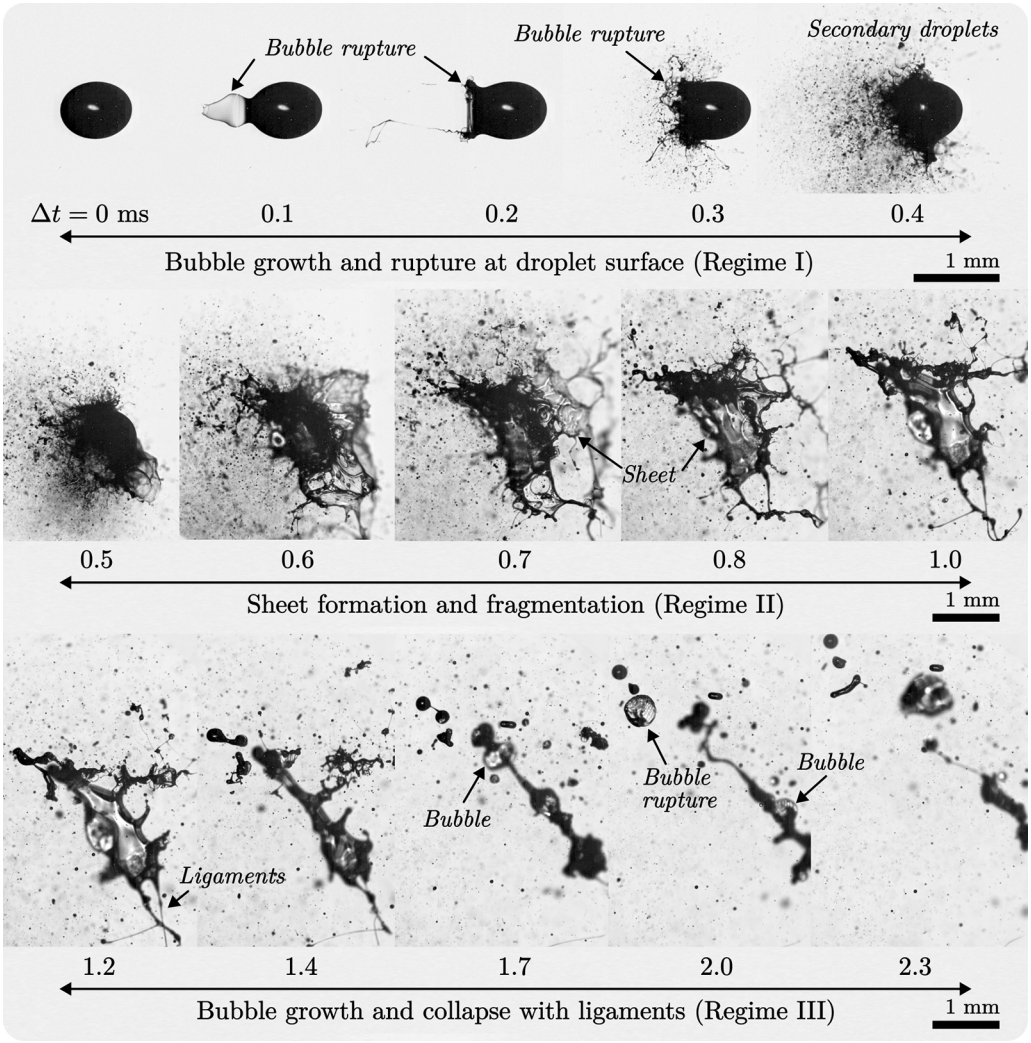

FIG. 5. *Breakup Type B*: Images showing temporal evolution of different regimes observed during *Type B* breakup of a xylene microemulsion droplet at $I^* = 0.8$. The timescale (Δt) is defined with respect to the bubble nucleation onset time (t_{onset}), such that $\Delta t = t - t_{\text{onset}}$. A complete video of the process is provided in the Supplemental Material [45] (see Video V2).

a temporally advanced stage of *Regime IV*. Due to the extremely high viscosity of the droplet at this stage, its collapse does not result in ligament ejection. As shown in Fig. 4, both regimes appear similar up to the point of collapse, differing primarily in their timescales.

In contrast to *Type A*, the *Type B* breakup mechanism exhibits three distinct regimes and occurs only under higher irradiation conditions ($I \geqslant 0.4$), observed particularly in xylene microemulsions. The breakup regimes begin with the nucleation of a single bubble near the droplet surface, which grows to a size smaller than the parent droplet ($D_{b,\max}/D_0 < 1$) and ruptures. This is followed by rapid nucleation and rupture of multiple surface bubbles that eject numerous secondary droplets, as shown in Fig. 5 (Regime I). This marks the *Regime I* of *Type B* breakup, with a characteristic timescale of $t_g \sim O(10^{-4}$ s) or shorter. Subsequently, rapid bubble growth from the droplet core stretches the liquid interface into a thin, unstable sheet. This stage defines *Regime II*, dominated

by sheet fragmentation. This rapid stretching and retraction of the sheet forms ligaments along its rim, which subsequently break into small droplets. The remaining liquid undergoes further bubble formation, and these bubbles eventually burst, producing fine secondary droplets. This stage corresponds to *Regime III* of the breakup *Type B*. It is to be noted that *Regime II* of this mechanism imparts a high momentum to the droplet, resulting in very short-duration dynamics (ending within $\Delta t \sim 2.5$ ms) compared to the *Type A* breakup.

The temporal evolution of the squared normalized droplet diameter, $(D/D_0)^2$, for two distinct breakup mechanisms, type A and B, is shown in Fig. 6(a) and 6(b), respectively. Each plot represents the sequence of laser-droplet interactions and the corresponding breakup regimes. *Type A* breakup progresses through five distinct regimes, whereas *Type B* exhibits three, both of which are reflected in the regression plots. In Type A, the onset of vapor nucleation (Regime I) is marked by a pronounced peak ($(D/D_0)^2 \sim 7.5$), corresponding to the rapid expansion of a large bubble, a characteristic of low irradiation conditions. The subsequent regimes can also be identified in the same plot, where smaller peaks associated with Regime II indicate comparatively smaller bubble growth dynamics. As discussed earlier, Regimes I and II proceed much faster than Regimes III, IV, and V, reflecting a transition from rapid vapor-driven expansion to slower, surfactant-controlled dynamics. Furthermore, the successive repetitive characteristics of the later Regimes are also reflected in the regression plot.

Figure 6(b) presents the temporal evolution for *Type B* breakup, observed for the xylene-based microemulsion at elevated irradiation intensities ($I^* \geqslant 0.4$). Compared with Type A, Type B exhibits a smaller initial peak (*Regime I*) at the onset, indicating growth of a smaller bubble ($D_{b,\max}/D_0 < 1$) near the droplet surface. This early-stage nucleation dynamics is shown more clearly in the inset of Fig. 6(b), which provides a magnified view of the temporal variation of $(D/D_0)^2$ in a narrow time window around $t \approx 148$–150 ms. It is evident that the initial peak corresponding to onset bubble nucleation is smaller $(D/D_0)^2 \sim 1.5$ in comparison to type A onset bubble [$(D/D_0)^2 \sim 7.5$]. The growth and rupture of this smaller surface bubble ($D_{b,\max}/D_0 < 1$) at nucleation onset marks the Regime I of *Type B* breakup. A noticeable reduction in the nucleation onset time ($t_{\text{onset}} \sim 150$ ms) is also observed, indicating accelerated phase change dynamics, likely resulting from enhanced energy absorption and a lower energy barrier for bubble formation for microemulsion (see Sec. III C). As time progresses, a prominent transient peak [$(D/D_0)^2 \sim 17.5$] is observed, corresponding to droplet breakup via liquid-sheet formation and subsequent fragmentation (see Fig. 5). This fragmentation process results in near-complete droplet disintegration and characterizes Regime II of Type B breakup. The smaller peaks that follow represent intermittent bubble growth and collapse events during the final breakup stages (*Regime III*).

Finally, *Type C* droplet breakup exhibits a hybrid morphology, inheriting characteristics of both *Type A* and *Type B* breakup mechanisms. The initial stage (i.e., *Regime I*) resembles the nucleation behavior observed in *Type B*, where a smaller bubble ($D_{b,\max}/D_0 < 1$) forms and grows at the onset. This behavior is also reflected in the regression plot as a smaller peak. As soon as the onset bubble ruptures, multiple smaller bubbles emerge and burst rapidly at the surface, ejecting numerous fine secondary droplets. All regimes of this breakup type are presented in Fig. 7, along with their corresponding signatures in the droplet regression plot. In this mechanism, *Regime II* involves the simultaneous growth of multiple bubbles that eventually coalesce into a much larger one [$(D_{b,\max}/D_0)^2 \sim 6.7$], in contrast to the *Regime II* of *Type A* breakup, where bubbles grow to smaller sizes and at a slower rate. This behavior is also reflected as a larger peak in the regression plot. Following this, the collapse of the bubble leads to the formation of the ligament, which further undergoes breakup and forms small secondary droplets, as shown in Fig. 7 (Regime IV). Similar to *Type A* breakup, this regime also involves ligament formation and breakup, but in *Type C*, the process is vigorous and produces a greater number of breakup events, hence secondary droplets. It is important to note that the apparent interaction between the breaking ligament and the collapsing bubble may influence the local breakup dynamics [see Fig 7 (Regime IV, $t = 36.3$ ms)]. In particular, partial coalescence between the ligament and the collapsing bubble could modify the atomization process by redistributing a fraction of the available energy toward interfacial merging

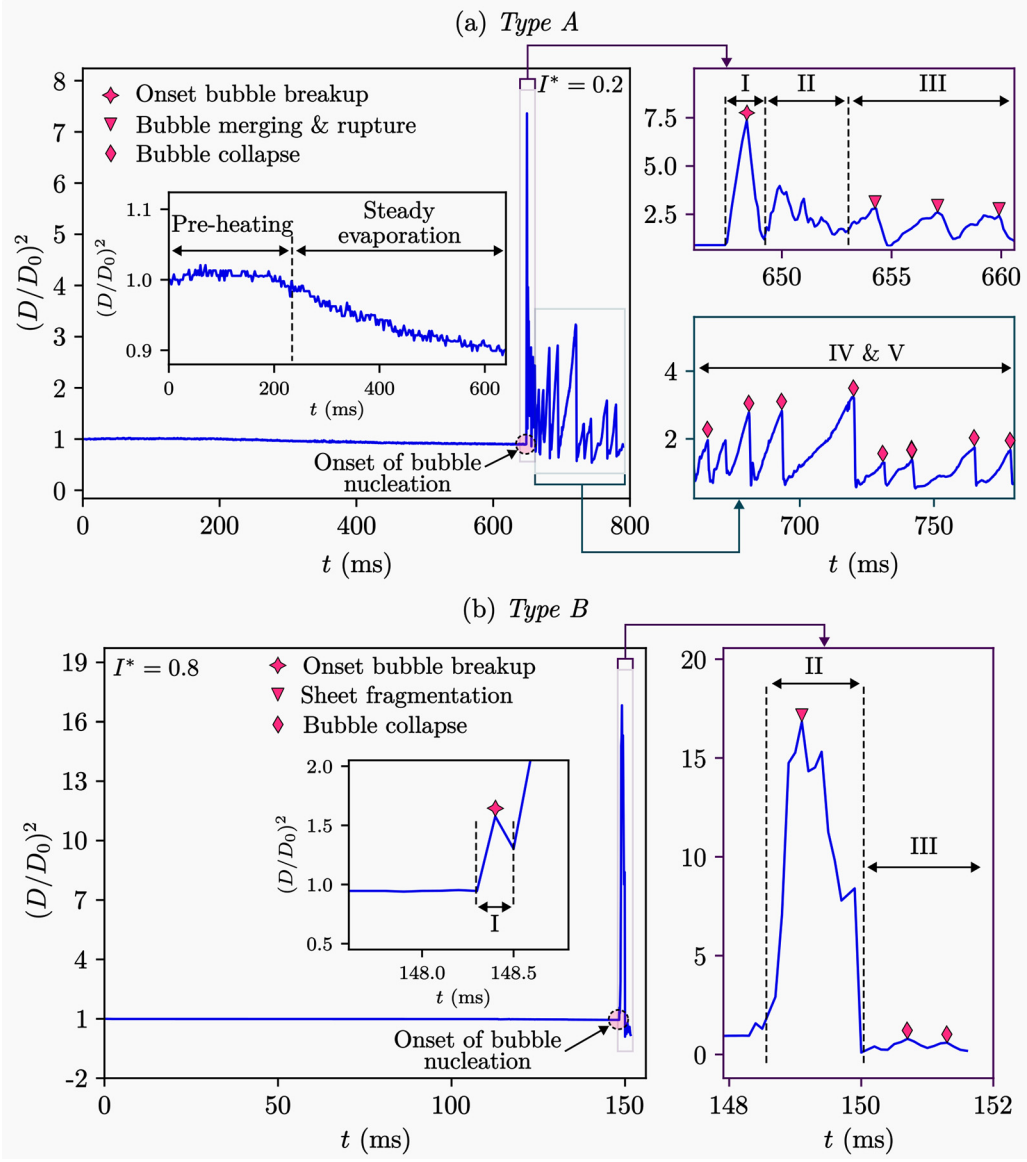

FIG. 6. Temporal evolution of normalized droplet diameter, $(D/D_0)^2$, for different breakup modes. (a) *Type A breakup* (decane, $I^* = 0.2$): The initial large peak corresponds to the growth of a single large bubble (*Regime I*) at the onset of nucleation. Subsequent smaller peaks (*Regime II*) represent multiple bubble growth and rupture events. The slower evolution of *Regimes III*, *IV*, and *V* is reflected, as are the repeated cycles of bubble growth and collapse characteristic at the later stages. (b) *Type B breakup* (xylene microemulsion, $I^* = 0.8$): In the inset, the initial smaller peak (*Regime I*) signifies the nucleation of a small surface bubble, followed by a dominant peak arising from unstable sheet formation and fragmentation (*Regime II*). The smaller peaks in *Regime III* correspond to repeated bubble growth and collapse events.

rather than fragmentation. However, such events were observed less frequently in the present experiments and therefore do not significantly affect the dominant breakup behavior reported. The final stage, *Regime V*, involves bubble growth and collapse without atomization, a behavior similar to *Type A* but occurring with a different growth rate. A key distinguishing observation is that, for

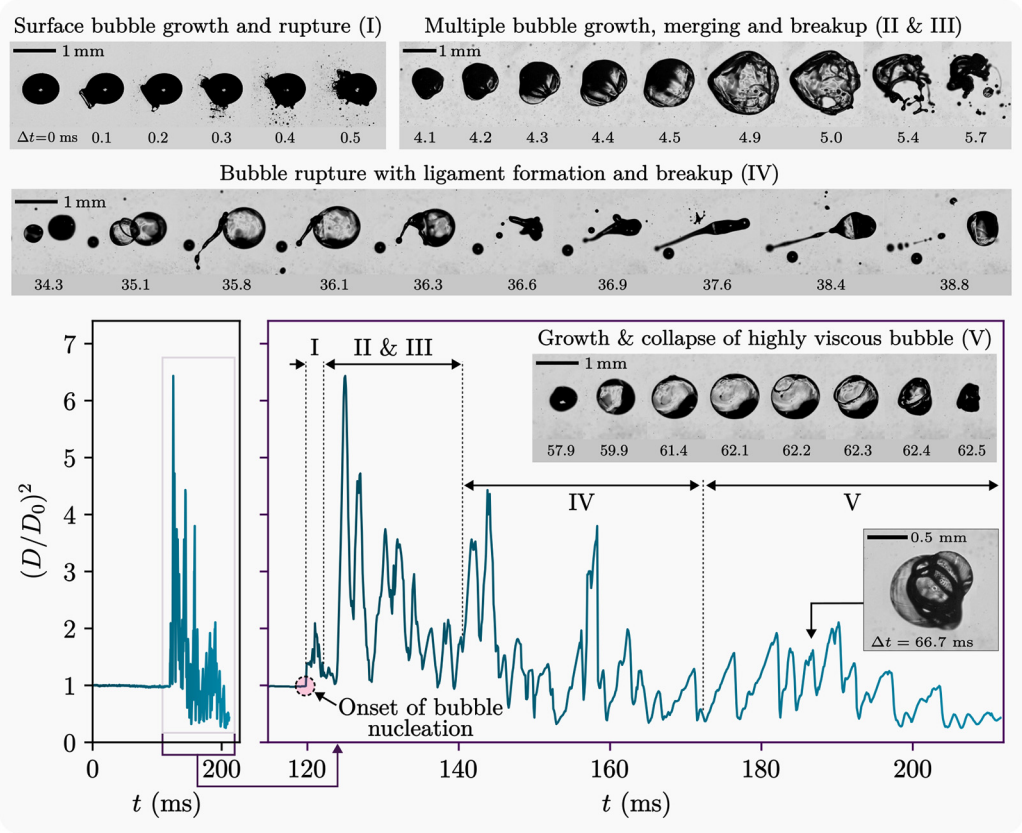

FIG. 7. Sequence of images corresponding to the five regimes (I, II, III, IV, and V) of *Type C* breakup are shown to illustrate the various modes of bubble rupture and collapse. The temporal evolution of the normalized droplet diameter during these regimes is shown, where each peak in the plot corresponds to a distinct bubble breakup mode, and the initial small peak at the onset of nucleation represents the growth of a small bubble. A complete video of the process is available in the Supplemental Material [45] (see Video V3).

Type C breakup, both single and multiple bubble growth and collapse cycles have been observed (see Fig. 7). However, *Type A* primarily shows a single bubble growth and collapse cycle. In both mechanisms, *Regime V* does not produce any secondary droplets, which is attributed to the increased viscosity of the droplet at this stage.

Most of the breakup stages observed in *Type C* are inherited from the *Type A* mechanism. The only deviation occurs in *Regime I*, which closely resembles the bubble nucleation and rupture dynamics of *Type B*. The characteristic timescales of bubble growth and breakup are significantly shorter than those in *Type A* breakup, primarily due to the higher heating rate. The detailed dynamics of bubble rupture and atomization within these regimes are discussed in the following sections.

A comparative summary of different breakup regimes observed among Type A, Type B, and Type C breakup mechanism is presented in Table III highlighting the key differences. In Regime I, all three types are characterized by the growth and rupture of a single bubble; however, their spatial origin and growth amplitude differ. Breakup is initiated by a single bubble. Type A exhibits bulk nucleation with $D_{b,\max}/D_0 > 1$, indicating that the bubble expands beyond the initial droplet diameter, resulting in strong volumetric expansion and violent disintegration. In contrast, Types B and C involve surface-localized bubbles with $D_{b,\max}/D_0 \lesssim 1$, where rupture occurs earlier. Regime II reveals clear divergence in breakup morphology. Type A transitions to multiple internal bubbles

TABLE III. Comparison of breakup regimes across different breakup Types, highlighting their key distinguishing features. The $D_{b,\max}/D_0$ denotes the maximum bubble diameter normalized by the initial droplet diameter attained prior to rupture.

Regime	Type A	Type B	Type C
I	Single bulk bubble growth and breakup $D_{b,\max}/D_0 > 1$	Single surface bubble growth and breakup $D_{b,\max}/D_0 \lesssim 1$	Single surface bubble growth and breakup $D_{b,\max}/D_0 \lesssim 1$
II	Multiple bubble growth and rupture $D_{b,\max}/D_0 < 1$	Breakup via Sheet formation $D_{b,\max}/D_0 \ll 1$	Multiple Bubble growth and merging $D_{b,\max}/D_0 > 1$
III	Bubble merging and collapse $D_{b,\max}/D_0 \lesssim 1$	Bubble growth and collapse $D_{b,\max}/D_0 < 1$	Bubble merging and breakup $D_{b,\max}/D_0 > 1$
IV	Bubble collapse and Ligaments mediated breakup $0.1 \lesssim D_{b,\max}/D_0 \lesssim 1$	–	Bubble collapse and Ligaments mediated breakup $0.1 \lesssim D_{b,\max}/D_0 \lesssim 1$
V	Bubble growth and collapse, no atomization $D_{b,\max}/D_0 \sim 1$	–	Bubble growth and collapse, no atomization $D_{b,\max}/D_0 \sim 1$

that grow and rupture with smaller sized bubbles ($D_{b,\max}/D_0 < 1$), leading to fragmentation and secondary droplets. Type B, however, shows sheet-mediated breakup with $D_{b,\max}/D_0 \ll 1$, where thin liquid films form and undergo fragmentation resulting in secondary droplets. In contrast, Type C exhibits multiple bubbles that grow, merge, and exceed the droplet scale ($D_{b,\max}/D_0 > 1$), producing larger bubbles prior to breakup.

In Regime III, Type A is dominated by bubble merging and collapse of the bubble with bubble size ($D_{b,\max}/D_0 \lesssim 1$) without atomization, Type B is characterized by bubble growth ($D_{b,\max}/D_0 < 1$) followed by collapse, leading to moderate atomization. In contrast, Type C involves bubble coalescence prior to rupture, with $D_{b,\max}/D_0 > 1$, and is associated with pronounced atomization. In Regime IV, ligament-mediated breakup occurs following bubble collapse with moderate bubble expansion ($0.1 \lesssim D_{b,\max}/D_0 \lesssim 1$). The ligaments generated in Type A exhibit lower kinetic energy and reduced instability growth compared to those in Type C. Regime V is characterized by bubble growth followed by collapse without atomization ($D_{b,\max}/D_0 \sim 1$). At this stage, the elevated effective viscosity suppresses interfacial instability growth, thereby preventing fragmentation. The detailed analysis of bubble growth and rupture mechanisms is presented in the subsequent section.

Figure 8 summarizes the temporal evolution of the square of the normalized droplet diameter $(D/D_0)^2$ for all microemulsion droplets under varying irradiation intensities, showing that differences in base oil and irradiation energy strongly influence the breakup and evaporation dynamics. The evaporation phase of the droplet is clearly distinguishable for all base oils except xylene. It is evident that the onset time of bubble nucleation decreases with increasing laser intensity. The multiple and repetitive characteristics of distinct regimes in *Type A* and *Type C* breakups are also evident, in contrast to the *Type B* breakup of xylene ($I^* \geqslant 0.4$), which exhibits a single sharp peak corresponding to a significantly shorter dynamics of its regimes.

Bubble-induced breakup in multicomponent droplets has been reported across binary mixtures, macroemulsions, nanofuels, and polymeric systems; however, the governing mechanisms differ fundamentally between these classes of droplets. In binary mixtures, disruptive burning is primarily driven by large volatility differentials, where homogeneous nucleation occurs under superheated conditions and breakup intensity scales with boiling-point disparity and volatile fraction [5,6]. In polymeric droplets, rupture is associated with solvent-evaporation-induced skin formation, where a viscoelastic interfacial layer confines the expanding vapor bubble and membrane inflation characteristics depend on irradiation intensity [33,50]. In contrast, burning nanoparticle-laden droplets exhibit

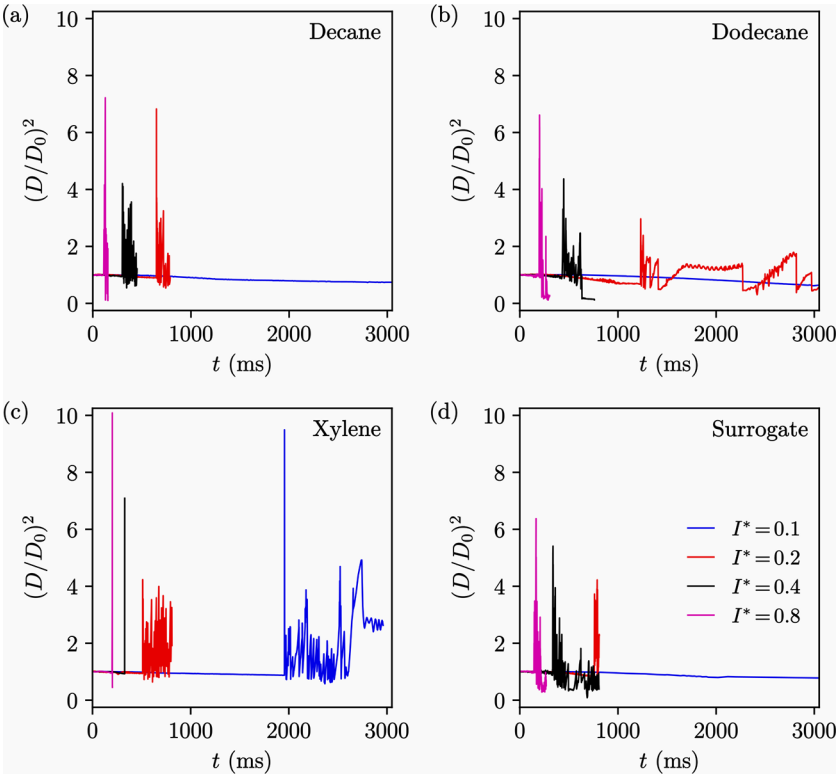

FIG. 8. Temporal variation of squared normalized droplet diameter, $(D/D_0)^2$, for microemulsions of different base oils: (a) decane, (b) dodecane, (c) xylene, and (d) surrogate, under varying laser irradiation intensities.

internal boiling initiated by nanoparticle aggregates, which serve as heterogeneous nucleation sites and promote ligament-dominated secondary atomization [10].

In contrast, the present observations suggest that bursting in microemulsion droplets may arise from nonstructural destabilization, wherein aggregation of surfactant molecules potentially facilitates heterogeneous nucleation. The bubble nucleation does not depend solely on volatility contrast, but on a heating-rate–controlled competition between volumetric laser energy deposition and acoustic-streaming–induced internal convection, which determines whether nucleation initiates symmetrically within the bulk or asymmetrically near the interface (as will be discussed later). A monotonically decreasing relationship has been observed between nucleation time and irradiation intensity. Various bubble breakup modes have been observed, which directly correlate to the associated bubble impact parameter β, undergoing breakup via various instabilities. For ligament-mediated breakup, a critical ligament aspect ratio AR $\sim \mathcal{O}(10^1)$ is identified as the transition threshold separating symmetric and asymmetric ligament breakup. Furthermore, progressive surfactant enrichment during evaporation modifies interfacial properties, altering collapse dynamics and ultimately suppressing atomization in the late stage of droplet evolution. While earlier studies have emphasized thermodynamic superheat, skin-layer formation, or nanoparticle-driven heterogeneous nucleation, we demonstrate that in microemulsions the critical bursting condition emerges from the coupled evolution of nanoscale internal structure, base oil properties, and heating rate. Additionally, a microemulsion droplet undergoes growth and rupture cascade of bubbles, showing distinct breakup modes depending on the heating rates and the internal property evolution, as will be discussed later.

C. Droplet heating and bubble nucleation

The interaction between a droplet of diameter D_0 and incident radiation of wavelength λ is governed by the Mie size parameter, $\alpha_M = \pi D_0/\lambda$, which determines the internal temperature distribution (i.e., slow/fast heating). Homogeneous volumetric heating occurs only when $\alpha_M < 1.5$, corresponding to droplets with $D_0 \leqslant 5.06\,\mu m$ [33,46], for IR wavelength of $\lambda = 10.6\,\mu m$. In the present experiments, the droplet diameter was $850\,\mu m$, far exceeding this limit, resulting in a nonuniform internal thermal field. However, this parameter only reflects the influence of droplet size relative to the beam diameter and irradiation wavelength, and does not account for the optical or thermal properties of the microemulsion, which strongly influence energy absorption and internal heat distribution. Furthermore, the irradiance intensity also plays a critical role in determining the droplet heating and subsequent breakup dynamics. However, based on the timescales, we can identify and distinguish between slow/fast heating regimes.

The fundamental energy equation for a droplet subjected to laser heating can be expressed as

$$\rho c_p\left(\frac{\partial T}{\partial t} + \mathbf{u}\cdot\nabla T\right) = \nabla\cdot(k\nabla T) + S, \tag{2}$$

where ρ, c_p, and k are the liquid density, specific heat, and thermal conductivity, respectively, and S represents the volumetric heat generation term due to laser absorption. The volumetric source term for laser heating is given as

$$S = \int q'''dV = \int \alpha_\lambda I(r,z)dV, \tag{3}$$

where α_λ is the absorption coefficient, $I(r,z)$ is the beam profile, dV is the differential volume. The differential volume is given by $dV = drdA$, where dr and dA represent the differential radial element and the differential area perpendicular to the laser propagation direction (z axis), respectively.

The left-hand side of Eq. (2) reflects the unsteady and convective transport terms, whereas the right-hand side includes thermal diffusion and the volumetric heat generation term. When this equation is integrated over the droplet volume, the convective term is neglected. As demonstrated by Gannena *et al.* [33], this is justified because, by assuming an incompressible flow ($\nabla\cdot u = 0$) and applying the Gauss Divergence Theorem (considering droplet interface as a Gaussian surface), the convective term is converted to a surface integral that evaluates to zero, as there is no internal liquid flow normal to the droplet interface. The thermal diffusion timescale, $t_d = \rho c_p D_0^2/k$, is significantly larger ($\mathcal{O}(10^1)$ seconds) than the onset of bubble nucleation (time before the first bubble nucleation is observed), t_{onset}, which is observed to be $\mathcal{O}(10^0)$ s for the lowest irradiation intensity. With increasing irradiation intensity, the onset time of nucleation decreases significantly. For instance, at $I^* = 0.8$, the nucleation occurs at $\mathcal{O}(10^{-1})$ s. Since thermal diffusion remains much slower than the nucleation process ($t_d \gg t_{onset}$), the diffusion term in Eq. (2) can be neglected. Therefore, volumetric heat generation is the most dominant term, and neglecting the convection and diffusion terms results in a modified energy equation as follows:

$$\iiint \rho c_p \frac{\partial T}{\partial t} dV = \iiint \alpha_\lambda I(r,z)dV. \tag{4}$$

Furthermore, by applying the Beer–Lambert law to account for irradiation attenuation during transmission through the material, the above equation can be expanded to the form reported by Gannena *et al.* [33]:

$$\frac{4\pi R^3 \rho c_p}{3}\frac{dT}{dt} = \pi\alpha_\lambda I_0 \int_0^{2R} e^{-\alpha_\lambda r}(2Rr - r^2)\,dr. \tag{5}$$

Integrating Eq. (5) yields the expression for the temporal evolution of the droplet temperature:

$$\frac{dT}{dt} = \frac{3I_0}{2\rho c_p}\zeta(R(t), \alpha_\lambda), \tag{6}$$

where $\zeta(R(t), \alpha_\lambda)$ is defined as

$$\zeta(R(t), \alpha_\lambda) = \frac{(\alpha_\lambda R - 1) + (\alpha_\lambda R + 1)e^{-\alpha_\lambda R}}{\alpha_\lambda^2 R^3}.$$

It is well-established that an intense flow field, known as acoustic streaming, is generated around an acoustically levitated droplet, with velocities that can reach up to 0.2 m/s. This external streaming induces a shear flow on the droplet's surface, which in turn drives internal toroidal vortices, as shown in previous studies [51,52]. This internal flow is critical as it promotes thermal homogenization within the droplet. In this work, we use the characteristic timescale of this internal convection (t_c) to differentiate between slow and fast heating regimes. To determine the t_c, we first calculate the internal velocity (u_d) using the relation [10,53]:

$$u_d = \sqrt{\frac{\rho_d \mu_d}{\rho_a \mu_a}} u_a, \tag{7}$$

where u_a is the ambient velocity, and ρ and μ are the density and viscosity of the droplet (d) and ambient air (a), respectively. The ambient velocity u_a is calculated from the Mach number (Ma) as $u_a = c_0 Ma$, where c_0 is the speed of sound. The Mach number is derived from the sound pressure level (SPL) of the levitator [51,54] via SPL(dB) = 197 + 20 log(Ma). We then estimate the convective timescale as $t_c = \pi D_0/u_d$. Based on this, we define the heating regime by comparing t_c to the bubble nucleation onset time (t_{onset}). The ratio of onset time to the convection timescale defines the slow/fast heating of droplet, such that fast heating is characterized when $t_{\text{onset}}/t_c \sim O(10^0)$, whereas slow heating corresponds to $t_{\text{onset}}/t_c \sim O(10^1)$ (a detailed discussion is presented later in this section).

As the droplet is heated, the interfacial tension between the base oil and dispersed water subdroplets increases [55] due to the detachment of AOT molecules from the interface, leading to an increase in the interfacial energy [2]. Additionally, the inherent sensitivity of microemulsions to compositional change (due to evaporation) consequently implies a change in their initial stable structure. The subsequent detachment of these individual AOT surfactant molecules can likely lead to self-assembly and aggregation of AOT within the microemulsion droplet. It is hypothesized that such aggregation may result in the formation of localized AOT clusters, which could act as heterogeneous nucleation sites, thereby lowering the activation energy barrier for phase transitions and facilitating the formation of vapor bubbles. We would also like to note that direct measurement of aggregation timescales or visualization of nanoscale surfactant clustering is beyond the spatiotemporal resolution of the current imaging techniques employed in the present study.

The nucleation onset time (t_{onset}) can be found by substituting the required degree of superheat (ΔT_{su}) into the heating rate equation:

$$\frac{\Delta T_{\text{su}}}{t_{\text{onset}}} \sim \frac{3I_0}{2\rho c_p}\zeta(R(t), \alpha_\lambda).$$

Rearranging for t_{onset} gives

$$t_{\text{onset}} \sim \frac{2\rho c_p \Delta T_{\text{su}}}{3I_0}\frac{1}{\zeta(R(t), \alpha_\lambda)}. \tag{8}$$

This result shows that the nucleation time is inversely proportional to the irradiation intensity (I_0). As shown in Fig. 9(a), the experimentally measured nucleation onset times are in reasonable agreement with the theoretical prediction given by Eq. (8). The value of constant C in the inverse function lies between 0.13–0.18 for all the microemulsions.

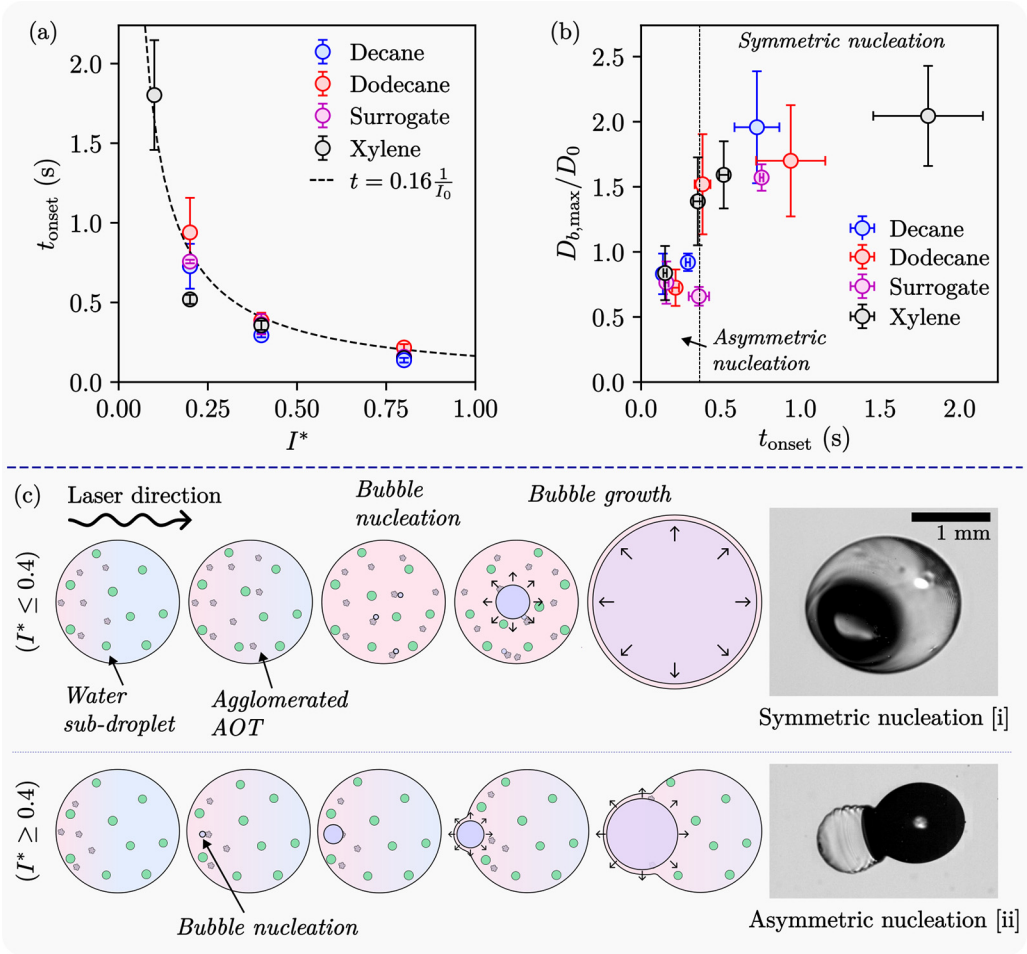

FIG. 9. (a) Dependence of the bubble nucleation time on the irradiation intensity, plotted for various microemulsion and compared with the theoretical relation given by Eq. (8). (b) The variation of the maximum bubble diameter, $D_{b,\max}$ attained by the first nucleated bubble (onset bubble) during its growth phase prior to rupture is shown as a function of nucleation time for the different microemulsions. (c) Schematic illustrating the two distinct bubble nucleation mechanisms (i) symmetric and (ii) asymmetric, observed inside the microemulsion droplet under slow and fast heating conditions.

Furthermore, the discrete water nanodroplets dispersed within the continuous oil phase of the microemulsion can potentially undergo homogeneous nucleation-induced vaporization. This process, wherein vapor nuclei form spontaneously within the liquid phase, presents a thermodynamically less favorable pathway compared to heterogeneous nucleation at preexisting interfaces, particularly under conditions of lower incident irradiance, where the requisite energy density for overcoming the critical nucleation energy barrier within the bulk liquid is less readily achieved. Analogous phenomena have been reported by Chaitanya *et al.* [32], wherein they demonstrated that the disparity in volatility between the aqueous and oil phases within an emulsion system facilitates homogeneous nucleation of the dispersed water component, contingent upon the attainment of a critical superheat threshold [32].

As mentioned earlier, Fig. 9(a) shows that the nucleation onset time, t_{onset}, decreases with increasing normalized irradiation intensity I^* for all base oils, exhibiting a clear inverse trend. Fig. 9(b)

presents the maximum bubble diameter normalized by the initial droplet diameter, $D_{b,\max}/D_0$, plotted against the nucleation onset time t_{onset}. Here, $D_{b,\max}$ refers to the maximum size attained by the first nucleated bubble during its growth phase prior to rupture. The x axis corresponds to the absolute nucleation onset time t_{onset}, measured from the beginning of laser irradiation (not the time elapsed after nucleation). A monotonic increase in $D_{b,\max}/D_0$ with increasing t_{onset} is observed, indicating that delayed nucleation (typically occurring at lower irradiation intensities) allows relatively higher thermal energy homogenization within the droplet, resulting in larger vapor before rupture (a detailed mechanism of bubble nucleation is discussed in the next paragraph). Conversely, for lower onset times smaller surface bubbles have been observed due to localized heating, undergoing asymmetric nucleation, as depicted in Fig. 9(b).

Figure 9(c) shows the two mechanisms for the initial bubble nucleation (i.e., onset bubble), which depend on the laser irradiation intensity. Once the first vapor bubble nucleates, it starts to grow over time due to the continuous irradiation from the laser. It is important to note that, in our observation, we only observe single bubble growth when the first bubble nucleates. However, in practicality, this bubble forms due to the coalescence of multiple very small bubbles inside the droplet, which are impossible to see due to experimental limitations [3]. We can observe the bubble only when they are of a significant size, depending on the experimental technique. These bubbles continue to grow over time and are observed to rupture at the droplet surface, resulting in various breakup events.

The symmetric breakup mode is characterized by the growth of a single vapor bubble ($D_{b,\max}$), whose maximum diameter significantly exceeds the droplet diameter at the onset of laser irradiation ($\beta \gtrsim \mathcal{O}(10^1)$). At lower heating rates ($I^* \leqslant 0.2$), droplets experience longer heating times ($t \sim \mathcal{O}(10^0)$), allowing the temperature to homogenize throughout the droplet. As discussed earlier, this temperature homogenization arises from vortical flow induced by acoustic streaming. At lower irradiation intensities, convective transport is relatively fast ($t_{\text{onset}}/t_c \sim \mathcal{O}(10^1)$), enabling efficient redistribution of thermal energy within the droplet. As a result, vapor nucleation is more likely to originate within the bulk of the droplet rather than near the interface. A bubble nucleating close to the droplet center has a larger surrounding liquid volume available for expansion, leading to the formation of a single, large vapor bubble. This mode of bubble growth is referred to as *symmetric* onset bubble growth, as it inflates the parent droplet uniformly, producing a nearly spherical bubble, as shown in Fig. 4 (Regime I). A schematic depiction is also presented in Figs. 9(c)[i] and 9(c)[ii] for symmetric and asymmetric bubble nucleation at the onset, respectively.

Asymmetric bubble nucleation is observed at higher heating rates, corresponding to short nucleation timescales ($t \sim \mathcal{O}(10^{-1})$) and preferential nucleation near the droplet surface. Owing to the high rate of energy deposition, the droplet attains the energy required for nucleation over a very short duration. Under these conditions, the heating process is highly localized and corresponds to the fast-heating regime ($t_{\text{onset}}/t_c \sim \mathcal{O}(10^0)$). Before thermal convection can homogenize the temperature within the droplet, the laser-facing side receives sufficient energy to trigger nucleation. This localized superheating results in bubble formation near the droplet interface rather than in the bulk, leading to asymmetric bubble growth. Since the bubble has limited liquid volume available for expansion on one side, its growth remains spatially confined, producing an asymmetric deformation of the parent droplet.

The distinction between symmetric and asymmetric nucleation is based on the three-axis centerline symmetry of the bubble at the onset of rupture. In the case of symmetric nucleation, the bubble completely engulfs the parent droplet, forming a nearly spherical bubble that exhibits symmetry about all three orthogonal axes. In contrast, when nucleation occurs near the droplet surface, the resulting bubble may exhibit symmetry about at most one axis but cannot achieve three-axis symmetry. This limitation arises because the parent droplet remains attached to the bubble, breaking geometric uniformity. All symmetry axes are defined with respect to the bubble center. It is to be noted that, in practice, perfect symmetry may not always be possible and visually evident due to slight off-center nucleation, partial thermal redistribution, or optical projection effects. Nevertheless, the underlying nucleation mechanism is dictated by whether energy deposition promotes bulk thermal homogenization or localized surface heating.

D. Atomization via different bubble breakup modes

Based on the experimental observations, the bubble size (D_b) significantly influences the breakup mode observed for microemulsions of different base oils and compositions. Five distinct modes of bubble bursting have been observed, which are categorized based on the bubble breakup parameter (β). The bubble breakup parameter is a nondimensional parameter defined as the ratio of the volume of the bubble just before the breakup to the initial droplet volume. It is expressed as

$$\beta \equiv \frac{\frac{\pi}{6}D_{b,\max}^3}{\frac{\pi}{6}D_0^3} = \left(\frac{D_{b,\max}}{D_0}\right)^3, \tag{9}$$

where $D_{b,\max}$ is the bubble diameter at the prebreakup instant and D_0 is the initial droplet diameter. Since β depends on the bubble volume, which in turn dictates the breakup mechanism, determines the strength of the bubble breakup and the degree of droplet deformation that ensues postbreakup (vapor release) [4,23]. Thus, the parameter β also governs the resulting ligament breakup dynamics and daughter droplet sizes during the breakup process, as discussed later in the manuscript. The diameter of the bubble at the prebreakup instant is denoted by $D_{b,\max}$, i.e., the maximum bubble diameter just before the breakup. The time instant at the onset of bubble nucleation is referred to as t_{onset} and the corresponding instantaneous droplet diameter is considered as the D_{onset} (onset droplet diameter). In fact, the bubble breakup parameter was originally defined as the ratio of bubble volume to the onset droplet volume in several studies [4,23,29], later modified by Priyadarshini *et al.* [3], which showed a better correlation with the experimental results for the combustion of microemulsion droplets.

It is important to recognize that the value of β is ultimately governed by the mechanisms that determine the maximum attainable bubble size $D_{b,\max}$ prior to rupture. The magnitude of $D_{b,\max}$ is not arbitrary; rather, it results from the coupled interaction between heating dynamics, nucleation location, and the evolving thermophysical properties of the droplet. The heating rate relative to the internal convective timescale dictates whether the droplet undergoes thermally homogenized (slow heating) or spatially localized (fast heating) superheating. Under slow-heating conditions, internal acoustic streaming–induced convection redistributes thermal energy throughout the droplet before nucleation. This promotes bulk nucleation and allows the bubble to expand quasi-spherically within a larger liquid confinement volume, thereby increasing $D_{b,\max}$ and consequently β. In contrast, fast heating leads to localized superheating near the irradiated surface. In this case, nucleation occurs closer to the interface, where geometric confinement and rapid film thinning limit bubble growth, resulting in smaller $D_{b,\max}$ and lower β. Consequently, the nucleation position within the droplet directly controls the available expansion volume for the bubble growth. A centrally nucleated bubble can grow to sizes much larger than the droplet diameter, resulting in the value of $\beta > 1$. Conversely, a surface-localized bubble is geometrically constrained and undergoes premature rupture due to asymmetric expansion and enhanced film thinning, leading to $\beta \lesssim 1$.

The thermophysical properties, such as surface tension and viscosity of the droplet and their temporal evolution arising from surfactant enrichment due to evaporation, also have a significant effect on the β. Bubble breakup occurs when the expanding film reaches a critical thickness or becomes unstable to capillary or shear-driven perturbations. Since the growth rates of these instabilities depend on σ and μ, the evolving material properties regulate the maximum bubble size attainable prior to rupture.

The value of β also determines the transition between the distinct breakup mechanisms (*Types A*, *B*, and *C*) observed experimentally, along with their distinct regime characteristics. For $\beta > O(1)$, the bubble expands to a size larger than the initial droplet size, leading to a symmetric bubble characteristic [see Fig. 9(c)]. Such β values are encountered in both *Type B* and *Type C* breakup. The distinction, however, emerges from the subsequent postnucleation evolution. In *Type B*, three regimes are identified, culminating primarily in sheet fragmentation. In contrast, *Type C* exhibits five distinct regimes, encompassing additional bubble breakup pathways, including ligament-mediated fragmentation and collapse of highly viscous bubbles at a later stage. It is worth mentioning that the

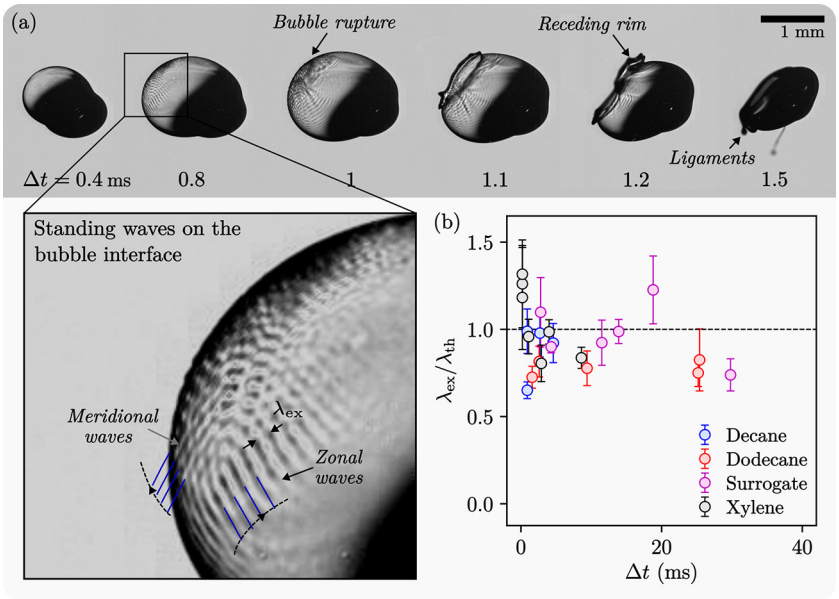

FIG. 10. (a) Sequence of images showing the evolution of capillary waves on the bubble interface leading to rupture of the bubble film. The magnified inset highlights the zonal and meridional waves on the bubble surface. (b) The ratio of experimentally and theoretically calculated wavelengths of capillary waves for different microemulsions is shown.

breakup types are classified based on the characteristics of the bubble at onset in conjunction with the subsequent regimes. The value of β alone is not sufficient to uniquely categorize the breakup mode. Nonetheless, β is a primary governing parameter that controls the bubble breakup modes under the aforementioned conditions, as elaborated in the subsequent sections.

1. Bubble rupture via Faraday waves and film drops ejection

As the bubble grows, ripples are observed on its surface, as shown in Fig. 10. These waves are typically observed during *Regime* I of *Type A* breakup, although they may also appear later in the subsequent stages. The influence of gravity on the droplet surface can be neglected as the wavelength ($\sim$40 μm) is significantly smaller than the bubble size ($\sim$1000–2500 μm). It can be inferred that these waves resemble the *capillary waves*, which are characterized by surface tension, density, and fluid inertia [23].

These capillary waves do not appear at the onset of nucleation; instead, they emerge when the bubble film thickness ($h_b \leqslant l_c$) is less than the capillary length scale ($l_c \sim \sqrt{\sigma/\rho g}$), as the capillary growth time decreases with film thickness, ($\tau_c \sim \sqrt{\rho h_b/\sigma}$). With time, the surface of the bubble develops a distinct craterlike complex pattern. This pattern results from the interaction of *zonal* and *meridional capillary waves*, which are produced in response to the acoustic field perpendicular to the zonal waves, as shown in Fig. 10. Rao *et al.* [23] reported a similar behavior on the bubble surface of an acoustically levitated water-in-oil *macroemulsion* droplet. These waves grow on the bubble surface, eventually leading to the rupture of the bubble film. This behavior has been confirmed through the experimental observations, which show that rupture consistently occurs where the wave complexity is most significant [see Fig. 10(a)].

The intense acoustic field generated around the suspended droplet modulates these capillary waves. These capillary waves are referred to as the *Faraday waves*, and their wavelength can be

calculated using the following relation [23,56]:

$$\lambda = \left(\frac{8\pi\sigma}{\rho f_0^2}\right)^{\frac{1}{3}}, \tag{10}$$

where σ is the surface tension, ρ is the density, and f_0 is the excitation frequency of sound waves generated by the acoustic levitator. The experimentally observed wavelength is compared with the wavelength predicted by Eq. 10 at the excitation frequency of the acoustic levitator (100 kHz), as shown in Fig. 10(b). The experimental wavelength is determined manually from the images by measuring the distance between the peaks of the dark bands immediately prior to rupture, when the wave pattern is most clearly identifiable. Such measurements require particular care due to the curvature of the spherical bubble, which can lead to the capture of projected lengths rather than the true wavelength. To minimize measurement uncertainty, the wavelength is measured at least 10 locations for a single wave-formation event leading to bubble rupture. Each data point in Fig. 10(b) represents the mean of these measurements, and the error bars correspond to the standard deviation from the mean. The uncertainties may also arise if bubble rupture occurs before the waves are fully developed. Furthermore, continuous evaporation during this stage can locally modify the liquid properties, which may, in turn, influence the development of these waves and introduce uncertainty in the final measured value. Nevertheless, the experimentally determined wavelength shows reasonable agreement with the theoretically calculated values. It should be noted that all theoretical calculations presented throughout the manuscript use the droplet properties listed in Table II, which represent the microemulsion properties under ambient conditions.

It is worth noting that here, two mechanisms contribute to the thinning of the bubble film. (1) As the bubble expands and grows in size, the film expands, which leads to thinning, and (2) simultaneously, the bubble film also evaporates continuously, which also contributes to the thinning of the bubble film. One might argue that, typically, evaporation is a phenomenon with a large timescale compared to bubble growth ($t_g \sim O(10^0)$ms), and its effect on film thinning could be neglected. However, it is also worth considering that the film is thin, and a small amount of mass loss can significantly affect the film thickness. Additionally, continuous heating can substantially enhance the evaporation. The effect of evaporation could be substantial, especially for liquids with very high vapor pressure (here, *p*-xylene exhibits a vapor pressure two orders of magnitude higher than the other base liquids considered). From Fig. 10(a), it can be seen that after the breakup, the receding rim does not develop the RT waves, and we see minimal ligaments at the end. For comparison (see Fig. 4 *Regime I*), we see many ligaments originating from the receding rim after bubble breakup. The suppression of these RT waves for xylene microemulsion is attributed to the evaporation of the liquid component, leading to an increase in the concentration of AOT on the bubble film. The higher concentration of these particulates leads to a highly viscous bubble film (which may also form a gel-like material if the desired concentration is reached), suppressing the growth of instabilities on the receding bubble surface. Hence, it can be inferred that evaporation plays a crucial role during bubble growth and film thinning, which ultimately affect the dynamics of bubble breakup.

The rupture of the bubble film leads to the formation of holes on the bubble surface, and once a hole forms, it undergoes expansion along the curved bubble surface. During the expansion, the rim of the hole collects the liquid; as a result, its thickness increases. The rim retracts along the curved bubble surface at the constant Taylor-Culick velocity (v_{rim}) [57–60]. This speed arises from a balance between surface tension and inertial forces and is given by

$$v_{\text{rim}} = \sqrt{\frac{2\sigma}{\rho h_b}}. \tag{11}$$

As the rim retracts along its curved path, the resulting centripetal acceleration ($a_{\text{rim}} = v_{\text{rim}}^2/R_b$) triggers a Rayleigh-Taylor instability, which destabilizes the rim. This instability drives the formation

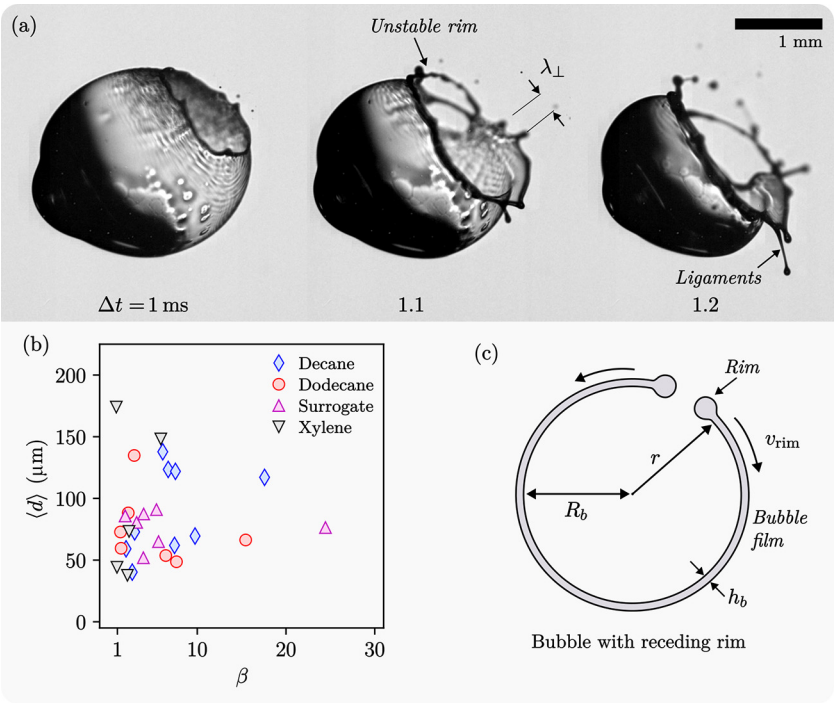

FIG. 11. (a) Temporal evolution of the unstable rim formed during bubble rupture, demonstrating the growth of Rayleigh-Taylor (RT) instability followed by secondary droplet formation driven by Plateau-Rayleigh instability.(b) Variation of the average size ($\langle d \rangle$) of secondary droplet as a function of the nondimensional breakup parameter, β. (c) Schematic showing the geometry of the liquid rim receding across the bubble surface with Taylor-Culick velocity.

and growth of wave-like undulations on the receding rim, causing it to fragment into ligaments. This process, however, only occurs if the residence time rim (T) on the cap exceeds the RT instability's characteristic growth time ($t_{\text{RT}} = \sqrt{\frac{\rho}{\sigma}}(R_b h_b)^{3/4}$) [61,62].

Subsequently, these ligaments become unstable and break apart into small droplets due to a secondary *Plateau-Rayleigh* instability, as depicted in Fig. 11. The inertial destabilization of a Rayleigh-Taylor type, which leads to the formation of ligaments, exhibits a wavelength that depends on the bubble size and the film thickness as $\lambda_\perp = \sqrt{R_b h_b}$ [61,62]. We observe the value $\lambda_\perp$ in the range of 0.4–1 mm, and they do not appear as regularly ordered as shown by Lhuissier *et al.* [61,63], which we attribute to the highly inhomogeneous film properties [see Fig. 11(b)].

The average size of droplets that get ejected from the destabilized rim depends on the bubble cap sand film thickness at burst h_b, as shown previously by Lhuissier *et al.* [61,63], as

$$d = \left(\frac{R_b^{13}}{\mathcal{L}^5}\right)^{\frac{1}{8}}. \tag{12}$$

This mechanism of droplet generation is observed for bubbles of larger size but small enough such that gravity can be neglected [62]. To accurately predict the droplet size, it is essential to know the length parameter $\mathcal{L}$. For the current system, it is challenging to determine its value accurately due to variations in its properties. Lhuissier *et al.* [63] refer to this as a "mystery length scale." In their experiments with water and soap solutions, they found that a value of 20 for this parameter effectively described their results. Here, we plot the average droplet size ($\langle d \rangle$) resulting from rim

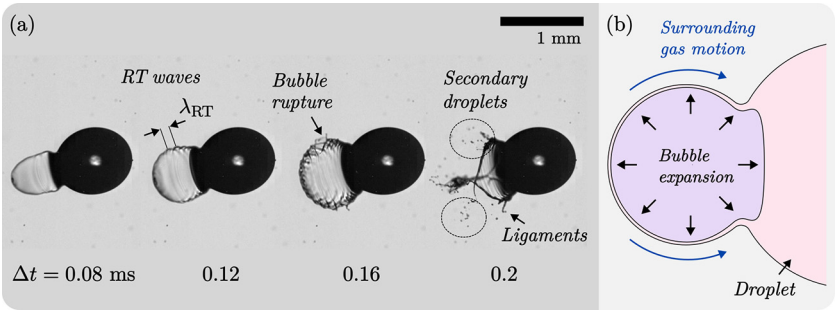

FIG. 12. Temporal evolution of bubble growth, showing the subsequent formation of Rayleigh-Taylor (RT) waves on the rapidly expanding bubble surface. These surface waves leads to the rupture of the bubble film leads to formation of ligament generating secondary droplets. (b) A schematic of the asymmetric bubble expansion leading to development of interfacial shear between bubble and surrounding gas.

breakup as a function of β. We observed that the average drop size increases with the value of β, as shown in Fig. 11(b).

2. Bubble rupture via RT instability

At higher heating rates ($I^* \geqslant 0.4$), the rapidly expanding bubble exhibits a distinct wave morphology on its surface, as shown in Fig. 12(a). While these interfacial patterns may suggest possible RT-KH coupling, the identification of KH contribution remains inferential and requires further investigation. The primary destabilization mechanism arises from the rapid vapor expansion within the bubble, which imposes a strong outward normal acceleration on the surrounding liquid film. This configuration is analogous to an RT instability, wherein a lighter fluid (vapor) accelerates a denser fluid (liquid), leading to amplification of interfacial perturbations. The imposed normal acceleration promotes the growth of characteristic RT-type waves on the thinning bubble film, ultimately facilitating rupture, as shown in Fig. 12.

In addition to the normal acceleration, the rapid unidirectional expansion of the bubble may induce a relative tangential motion between the expanding liquid film and the surrounding gas, thereby generating interfacial shear. A schematic illustrating the bubble expansion and the induced motion of the surrounding gas is presented in Fig. 12(b). In principle, such shear could promote a KH-type instability if it becomes sufficiently strong to overcome the stabilizing influences of surface tension and viscous damping. This could potentially contribute to the rupture of the bubble; however, the present study does not provide direct quantitative evidence to substantiate the occurrence of KH instability under the examined conditions. Therefore, the current analysis is restricted to RT-driven wave growth, which is directly supported by the observed acceleration-dominated dynamics. The possible role of KH-type shear instability remains speculative and warrants dedicated future investigation.

Once the bubble surface ruptures, a similar mechanism of receding rim destabilization follows as discussed in Sec. III D 1. The destabilized rim eventually leads to the formation of tiny secondary droplets. The calculated wavelength of the RT wave resulting from the rapid expansion of the bubble can be determined using the following relation:

$$\lambda_{RT} = 2\pi\sqrt{\frac{3\sigma}{\rho a_b}}, \tag{13}$$

where a_b is the acceleration of the bubble expansion. The experimentally measured wavelength was determined to be of the order $\lambda \sim 90 \pm 15\,\mu$m, and the theoretical wavelength calculated using Eq. (13) predicted a value of $\sim$200 μm. Although there is a quantitative difference between the

measured and predicted values, the experimental and theoretical results are of the same order of magnitude. It is important to emphasize that the predicted values are calculated using the system's initial properties at $t = 0$. However, this assumption does not hold in the experiment, which is a highly dynamic process. The droplet's physical properties, such as its composition, viscosity, and surface tension, are not constant; they evolve continuously as the volatile components evaporate. These properties also depend on the local temperature, which further increases the complexity of the problem. Thus, this temporal variation of the governing properties makes an accurate, time-dependent prediction exceptionally difficult. Once the bubble film is ruptured, the receding rim breaks into tiny droplets of size in the range $d \sim 10$–$25\,\mu$m.

3. Bubble rupture with ligament-mediated atomization

Rupture of a bubble leads to the formation of a spherical cavity. As this cavity collapses under the influence of surface tension, it ejects a jet from within, known as a ligament. The length of this ligament increases with time, and given sufficient kinetic energy, the ligament breaks into several secondary droplets. The bubble film rupture occurs spontaneously or can be induced by the previously discussed instabilities. Upon rupture, the bubble transforms into an open cavity, allowing the pressurized vapor inside the cavity to escape. This rapid vapor expulsion creates a low-pressure region inside the bubble, opposite the rupture point. Simultaneously, surface tension drives the rapid recession of the ruptured film in the opposite direction of the vapor expulsion. The combined effect of surface tension-driven retraction and vapor expulsion causes a ligament to be ejected from the bubble cavity. The cavity collapse, ligament ejection, and subsequent secondary droplet formation observed here show qualitative resemblance to the bursting dynamics reported for reactive droplets by Inoue *et al.* [24] and for combusting blended-fuel droplets by Rao *et al.* [49], despite the fundamentally different physicochemical nature of those systems compared with the present laser-heated microemulsion droplets. A sequence of images depicting the process of cavity collapse leading to the formation of a jet is shown in Fig. 13(a) for the nonbreakup case. It can be observed that the rupture of the bubble leads to the collapse of the cavity ($\Delta t \sim 178.7$–179.4 ms), and later a ligament ejects out from the cavity ($\Delta t \sim 179.6$ ms), and then the ligament size increases with time and subsequently retracts ($\Delta t \sim 179.8$–182.4 ms). Typically, the ligament-mediated breakup of bubbles has been observed for $\beta \sim \mathcal{O}(10^{-3})$–$\mathcal{O}(10^{0})$.

The ligament aspect ratio (AR) has been demonstrated in numerous prior studies [3,5,6,29,64–66] to be a critical parameter for understanding and predicting the dynamics of liquid jets and their subsequent fragmentation.

The ligament aspect ratio is defined as the ratio of the ligament's length to its diameter:

$$\mathrm{AR} = \frac{L}{\xi(L)}, \tag{14}$$

where L is the length and ξ is the diameter of the ligament, which varies along the ligament length. The dynamics of ligament breakup are dictated by the balance between the destabilizing influence of the inertia force (which can trigger the Plateau-Rayleigh instability) and the stabilizing effects arising from viscosity and surface tension. It is evident that ligaments with higher-energy tend to elongate more and exhibit a smaller diameter. Thus, the aspect ratio serves as a fundamental nondimensional characteristic that governs the stability of the ejected ligament. The aspect ratio of the ligament was determined by simultaneously calculating its length and its neck diameter at the point of maximum extension. The regression plots presented in Figs. 13(b) and 13(c) illustrate the temporal evolution of bubble collapse and subsequent ligament formation, highlighting the distinct behavior observed in the nonbreakup and breakup cases, respectively. The insets in Figs. 13(b) and 13(c) represent the variation of aspect ratio as the ligament evolves with time for the ligament nonbreakup and breakup cases, respectively. It can be observed that, for the nonbreakup case, the aspect ratio initially increases, reaches a peak, and subsequently decreases with time. In contrast,

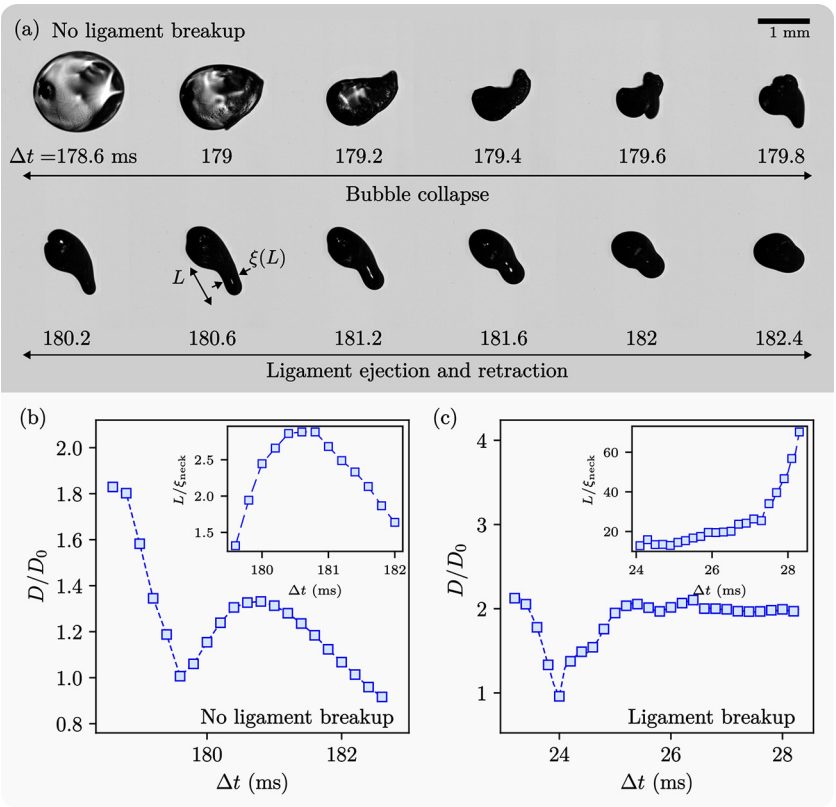

FIG. 13. (a) Image sequence illustrating the physical process of bubble collapse and ligament ejection for the nonbreakup case. (b) and (c) Temporal plots showing the bubble size variation with time for the nonbreakup and breakup cases, respectively. The inset plots [in panels (b) and (c)] further detail the corresponding variation of the average aspect ratio (AR) of the ligament with time for the respective cases.

for the breakup case, the aspect ratio continues to increase until the ligament breaks into secondary droplets.

The sequence of images depicting ligament breakup is presented in Fig. 14. The images illustrate three distinct stages of the breakup dynamics: (1) bubble rupture and collapse, (2) ligament ejection followed by end pinch-off (i.e., asymmetric ligament breakup), and (3) ligament retraction leading to symmetric pinch-off (i.e., symmetric ligament breakup). As shown, two primary breakup mechanisms are identified, i.e., symmetric and asymmetric. The symmetric breakup occurs when the ligament undergoes complete axial stretching before fragmenting into multiple secondary droplets. In contrast, the asymmetric breakup takes place when a single droplet pinches off from one end of the ligament, while the remaining portion retracts without undergoing further breakup. However, both types of breakup can coexist, as illustrated in Fig. 14.

To elucidate the dynamics of bubble collapse and ligament breakup, the ligament aspect ratio (AR) is plotted against the bubble breakup impact parameter (β), as shown in Fig. 15. A critical ligament aspect ratio of AR $\sim \mathcal{O}(10^1)$ is observed to demarcate the transition between the nonbreakup and breakup regimes. For AR $< \mathcal{O}(10^1)$ (green-shaded region), the ligament remains stable and does not undergo secondary fragmentation, whereas for AR $> \mathcal{O}(10^1)$ (red-shaded region), breakup becomes increasingly probable. The breakup of a liquid ligament is governed by its aspect ratio (AR) and the Ohnesorge number (Oh), as established in previous studies [64–66]. Schulkes [64] showed that a filament with Oh $\geqslant \mathcal{O}(1)$ will retract into a single droplet irrespective of its

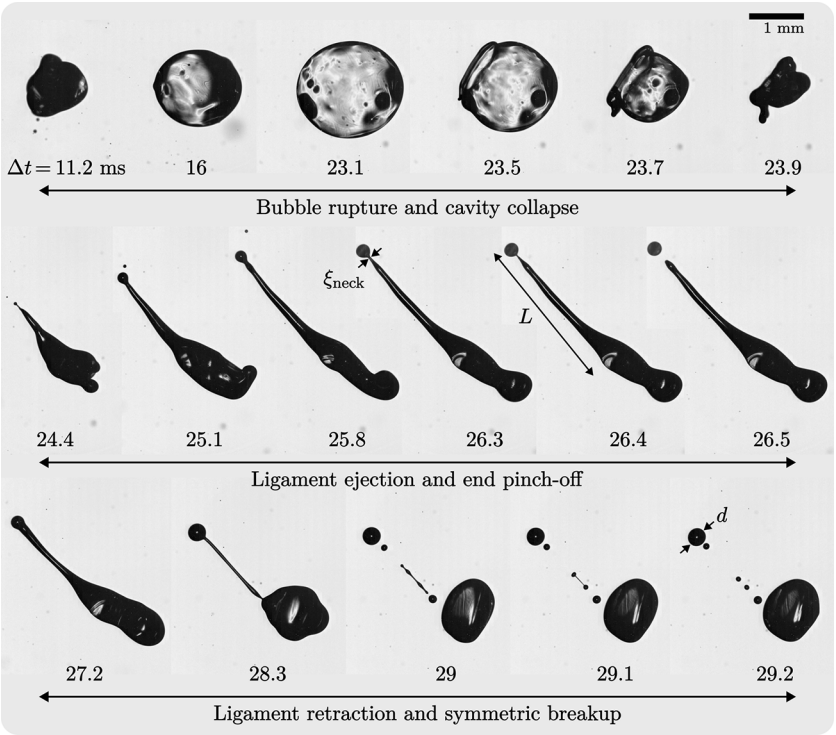

FIG. 14. Sequence of images illustrating the formation of a high aspect ratio ligament generated during bubble collapse. The process initiates with bubble rupture and cavity collapse, followed by ligament ejection, end pinch-off, and subsequent ligament retraction leading to a symmetric pinch-off, generating small droplets.

aspect ratio. In contrast, sufficiently long filaments with Oh $\leqslant \mathcal{O}(0.01)$ develop bulges connected by thinning necks, which ultimately pinch off to form separate droplets. Notz and Basaran [65] further demonstrated that, in the low-Ohnesorge-number regime (Oh $\leqslant \mathcal{O}(1)$), the ultimate breakup of a liquid filament is controlled jointly by a critical Ohnesorge number and a critical AR, both of

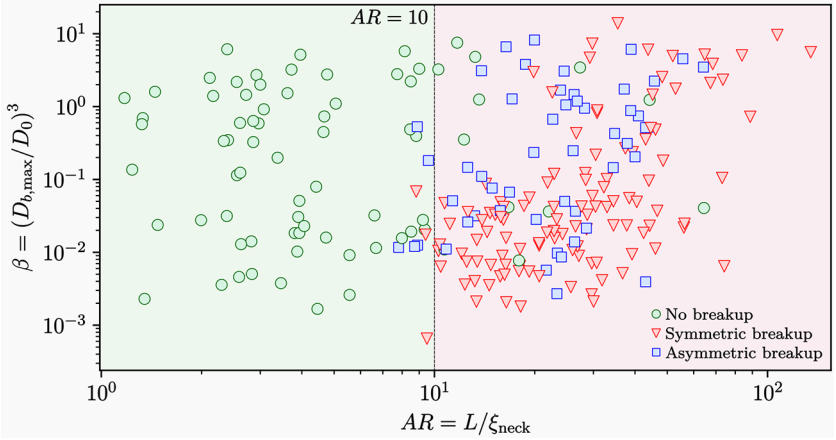

FIG. 15. Variation of the breakup impact parameter β with the ligament aspect ratio (AR), indicating the critical aspect ratio required for ligament breakup.

which determine whether the filament retracts or undergoes breakup. This framework is consistent with our experimental observations and agrees with the findings of Castrejón-Pita *et al.* [66], who reported ligament breakup occurring near a critical aspect ratio of AR $\approx 6 \pm 1$, thereby supporting the existence of a well-defined geometric threshold for capillary-driven fragmentation.

It can be observed that (see Fig. 15), in the nonbreakup region (shaded in green), the values of β are distributed with reasonable uniformity across a vast range $\sim\mathcal{O}(10^{-3}$–$10^{1})$. As shown in Fig. 15, within the nonbreakup region (shaded in green), the values of β are distributed relatively uniformly over a broad range, approximately $\sim\mathcal{O}(10^{-3}$–$10^{1})$. This distribution indicates that bubble size alone does not govern the breakup process. This behavior can be attributed to the dynamically evolving fluid properties resulting from continuous heating, as well as the underlying mechanism of cavity collapse. The dynamics of bubble collapse is governed by the interplay between the restoring surface tension and the inertia of the pressurized vapor as it is rapidly expelled. Unlike bubble collapse in a quiescent liquid pool, where the internal pressure is balanced by surface tension and the rupture dynamics are primarily governed by gravitational drainage of the thin film [62]. In our case, however, the system is not in equilibrium; the internal capillary pressure exceeds the confining surface tension pressure ($\Delta p_b \geqslant \kappa\sigma$), where κ denotes the curvature of the bubble. Furthermore, continuous external heating significantly influences the breakup dynamics of the bubble by elevating the internal vapor pressure. The resulting pressure rise increases the vapor expulsion velocity during collapse, leading to the formation of a high-momentum liquid ligament. Such a ligament experiences enhanced stretching, resulting in an increased aspect ratio, and is more likely to undergo secondary breakup.

It can also be observed from Fig. 15 that, within the breakup region (shaded in red), the asymmetric breakup data points exhibit a significantly wider scatter in β, whereas the symmetric breakup cases are predominantly confined to the range $\beta \sim \mathcal{O}(10^{-1})$–$\mathcal{O}(10^{-3})$. As mentioned earlier, symmetric breakup refers to ligament stretching into a single liquid thread that subsequently disintegrates into multiple small secondary droplets. In contrast, asymmetric breakup is characterized by the pinch-off of a single small droplet from the ligament tip, while the remaining portion retracts to form a larger droplet. This distinct behavior can be attributed to the variation in bubble size and its influence on internal pressure. Smaller bubbles possess a higher curvature, which, according to the Young–Laplace relation, results in an elevated internal pressure. The increased bubble pressure enhances the expulsion velocity of the vapor jet during collapse, leading to the formation of more energetic ligaments that are more likely to undergo symmetric breakup. Conversely, larger bubbles with lower internal pressure generate relatively slower and more stable ligaments, favoring symmetric breakup modes.

To distinguish between symmetric and asymmetric ligament breakup, we further examine the velocity and timescales associated with ligament evolution. The breakup dynamics are primarily governed by the competition between the inertial forces of the ejected ligament and the restoring action of surface tension. To quantify the relative significance of these effects, we evaluate the ligament Weber number based on its average diameter, defined as

$$\mathrm{We}_{\xi} = \frac{\rho V^2 \xi}{\sigma}, \tag{15}$$

where ρ is the liquid density, V is the characteristic ejection velocity, ξ is the ligament diameter, and σ is the surface tension. A higher Weber number indicates that inertial effects dominate over surface tension, favoring ligament stretching and subsequent breakup. In contrast, a lower Weber number corresponds to cases where surface tension resists deformation, promoting ligament stability and symmetric retraction. The variation of the Weber number with the bubble breakup impact parameter (β) is presented in Fig. 16(a). It can be observed that bubbles of smaller size exhibit relatively higher Weber numbers, which correspond to conditions favorable for symmetric breakup. In contrast, larger bubbles tend to exhibit lower Weber numbers, as the internal pressure and resulting vapor expulsion velocity are comparatively smaller, leading to asymmetric ligament breakup. It is to be noted that the dynamics of ligament breakup are also influenced by the continuously evolving thermophysical

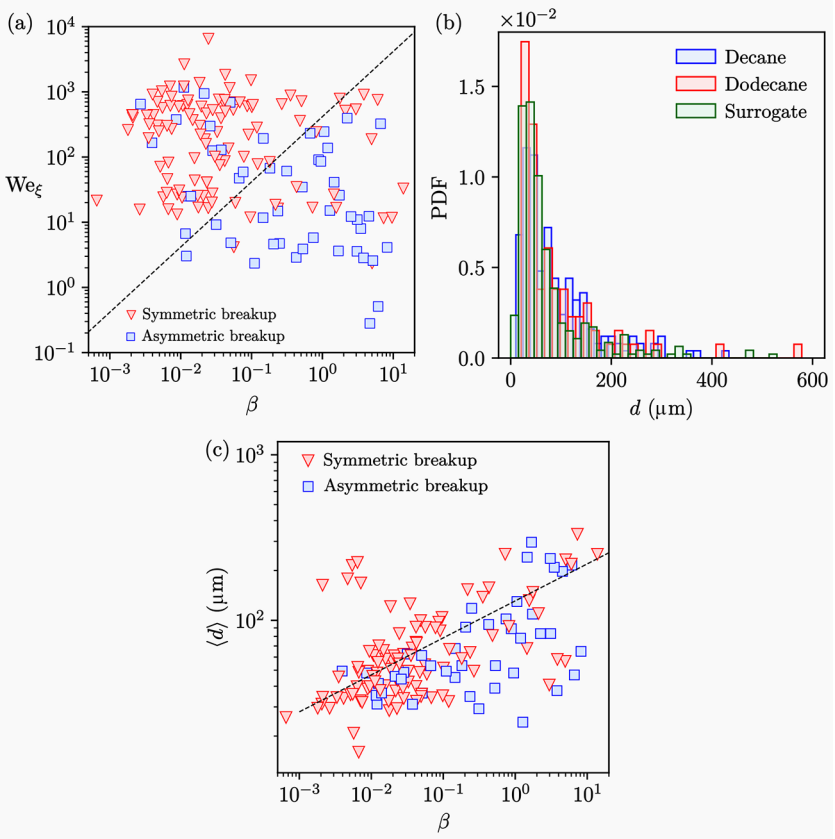

FIG. 16. (a) Variation of the ligament Weber number with the breakup impact parameter, differentiating between symmetric and asymmetric ligament breakup. (b) The probability density function of the secondary droplet size distribution is also shown for different microemulsions. (c) Variation of average secondary droplet size (d) with β generated during ligament breakup.

properties of the liquid during heating. As the temperature rises, variations in viscosity, surface tension, and vapor pressure significantly alter the force balance governing ligament formation and fragmentation. These dynamically changing properties can modify the relative dominance of inertial and capillary effects, thereby influencing the mode and timescale of breakup. Consequently, the continuous heating introduces additional complexity into the ligament evolution process.

The bubble breakup parameter β is defined as the ratio of the maximum bubble volume to the droplet volume and physically sets the characteristic cavity size at the instant of rupture. Upon rupture, the bubble transforms into an open cavity, whose subsequent collapse generates the ejected ligament [Fig. 13(a)]. The cavity radius at rupture determines the interfacial curvature $\kappa \sim 1/R_b$ and the associated capillary pressure gradient. Thus, a smaller value of β corresponds to smaller cavity radii and hence higher curvature. According to the Young–Laplace relation, this results in larger capillary pressure gradients, which produce stronger acceleration during collapse. The enhanced acceleration results in a thinner, more rapidly stretched ligament, thereby increasing the aspect ratio. Conversely, larger values of β correspond to larger cavities with lower curvature and reduced pressure gradients. In this case, collapse proceeds over a larger length scale, generating comparatively thicker ligaments with smaller AR. This trend is consistent with the experimental data shown in Fig. 15, where higher AR values are predominantly associated with lower values of $\beta \sim \mathcal{O}(10^{-1}$–$10^{-3})$. Furthermore, the ligament Weber number plotted in Fig. 16(a) shows that

smaller bubbles exhibit higher momentum ligaments, resulting in symmetric ligament breakup, supporting the curvature-based argument. The combined AR $-\beta$ and $\mathrm{We}_\xi - \beta$ trends confirm that β governs ligament aspect ratio through its control of the collapse length scale and curvature-driven acceleration. It is also important to account for the influence of transiently varying thermophysical properties. Under such conditions, even smaller β values may produce comparatively less energetic ligaments. This interpretation is consistent with the experimental observations shown in Figs. 15 and 16(a), where the data points display appreciable scatter rather than collapsing into distinctly separated regions defined solely by β.

The droplet size distribution corresponding to ligament breakup is presented in Fig. 16(b). It can be observed that most of the ejected droplets fall within the size range of $d \sim 20$–$100\,\mu\mathrm{m}$, resulting from the fragmentation of the ligaments. It is important to note that the breakup dynamics strongly depend on the heating rate and the fluid properties. Most bubble breakup events leading to atomization occur during the early stages, when sufficient liquid remains within the droplet. Once the droplet loses excessive liquid, its viscosity increases, and the subsequent cavity collapse no longer results in breakup. This transition gives rise to a new regime of bubble collapse, which is discussed in Sec. III E.

The statistics of the daughter droplets are governed by the characteristic diameter of the ejected ligament, which in turn is controlled by the bubble breakup parameter β. Since the ligament diameter ξ is set by the collapse length scale of the cavity, smaller values of β (corresponding to smaller cavity radii and higher curvature) generate thinner ligaments. According to classical capillary breakup theory, the characteristic droplet diameter produced by Plateau-Rayleigh instability scales with the ligament diameter, i.e., $d \sim \mathcal{O}(\xi)$. Consequently, lower β values lead to the formation of smaller secondary droplets, whereas larger β values produce thicker ligaments that fragment into comparatively larger droplets.

The dependence of the daughter droplet statistics on β is illustrated in Fig. 16(c), where the average secondary droplet diameter $\langle d \rangle$ is plotted as a function of the bubble breakup parameter β. An increase in average droplet size is observed over the range $\beta \sim \mathcal{O}(10^{-3}$–$10^{1})$. This trend indicates that larger bubble expansion relative to the droplet size results in systematically larger daughter droplets. Since β determines the maximum cavity radius at rupture, it sets the characteristic collapse length scale and, consequently, the ligament diameter ξ. These trends are consistent with previously reported studies [3,5,62]. Although some scatter is present, which can be attributed to the continuously evolving thermophysical properties and heating conditions, the overall positive correlation confirms that β governs the daughter droplet statistics by controlling the collapse geometry and ligament thickness. In addition, continuous heating during the breakup process can induce bubble nucleation within the daughter droplets, thereby increasing the apparent measured droplet size. Although careful procedures were followed during droplet size measurements and droplets containing visibly resolvable bubbles were excluded from the analysis, it is possible that some droplets contained microbubbles that were not detectable. The presence of such undetected bubbles may introduce uncertainty in the measured daughter droplet diameters and, consequently, affect the accuracy of the reported data.

4. Droplet breakup via sheet formation

Figure 17 illustrates the sequence of events leading to droplet breakup via liquid sheet formation, observed during *Regime II* of the *Type B* breakup mechanism. Following the initial bubble nucleation and rupture near the droplet surface (*Regime I*), the breakup of a high-pressure subsurface bubble generates a rapidly expanding liquid sheet, with an estimated expansion velocity of $\sim\mathcal{O}(10^{1})$ m/s. Similar bubble-induced sheet formations have been reported in macroemulsions [23,32] and evaporating polymeric droplets [33], where intense bubble breakup drives strong interfacial acceleration, producing thin liquid sheets that subsequently fragment. This behavior can be attributed to the breakup of small, high-pressure bubbles ($\beta \ll \mathcal{O}1$), whose breakup releases sufficient energy to eject the surrounding liquid into a sheet-like structure. The pressure force generated during

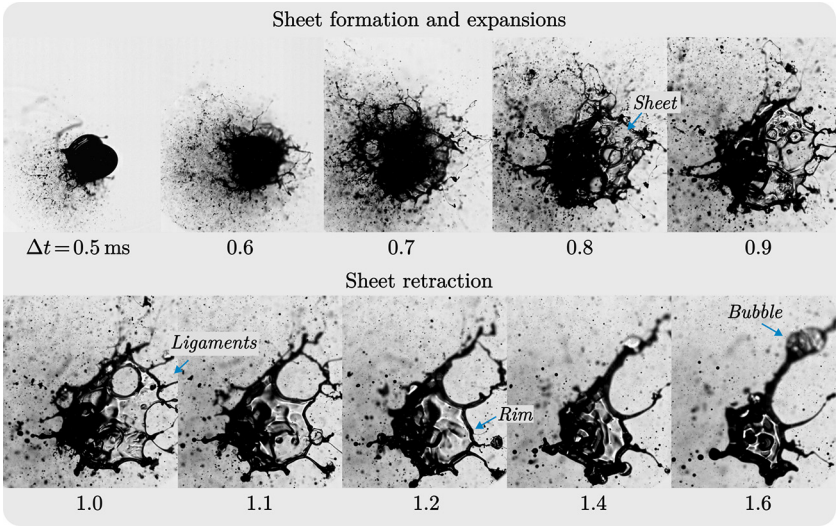

FIG. 17. Sequence of images showing droplet breakup via sheet fragmentation, illustrating sheet expansion and retraction, followed by rim ligament formation and their subsequent disintegration into smaller droplets.

bubble rupture can be estimated as $F_b \sim (p_b - p_a)\pi D_b^2/6$, where p_b and p_a denote the internal and ambient pressures, respectively, and D_b is the bubble diameter at the onset of breakup. This breakup mode is typically observed at higher normalized irradiation intensities ($I^* \geqslant 0.4$) for xylene-based microemulsions.

The rapid bubble breakup induces strong recoil and can completely disintegrate the parent droplet, imparting a significant propulsive force. The evolution of this process is shown in Figs. 17 and 5. During expansion, the liquid sheet accelerates rapidly, with a characteristic timescale of approximately 0.3 ms. As the sheet grows outward, it becomes unstable to RT instabilities due to the rapid acceleration of this sheet. Following its expansion, the sheet undergoes retraction driven by the opposing force of surface tension. During this relatively slow retraction ($\sim\mathcal{O}(10^0)$ ms), liquid accumulates along the periphery of the sheet, leading to the formation of a thickened rim (as shown in Fig. 17). This rim subsequently destabilizes, stretching into ligaments that elongate and ultimately disintegrate via the Rayleigh–Plateau instability, generating fine secondary droplets.

E. Growth and collapse of highly viscous bubbles

As time progresses, continuous vaporization of the volatile components leads to progressive depletion of the liquid phase. Owing to the nonvolatile nature of the surfactant (AOT), its relative concentration within the droplet increases steadily. This enrichment promotes spatial compositional change and aggregation of surfactant molecules. In the shadowgraph images, low-reflectivity regions (dark patches) are observed on the bubble interface, particularly at the later stages (Regimes III to V). Bubble expansion driven by continued vaporization further intensifies interfacial surfactant enrichment, leading to localized compositional heterogeneity and the development of surfactant-rich domains along the bubble film. At this stage, diffusion-driven homogenization of these particles becomes increasingly unfavorable due to its inherently slow timescale and further inhibition due to elevated viscosity. A clear distinction in bubble reflectivity can be observed when comparing bubbles of Regime I in type A breakup in Figs. 4 and 18 (Regime V, Type A). Since shadowgraph contrast arises from spatial gradients in refractive index, such surfactant-rich thicker regions would produce localized optical inhomogeneities and therefore appear as dark regions.

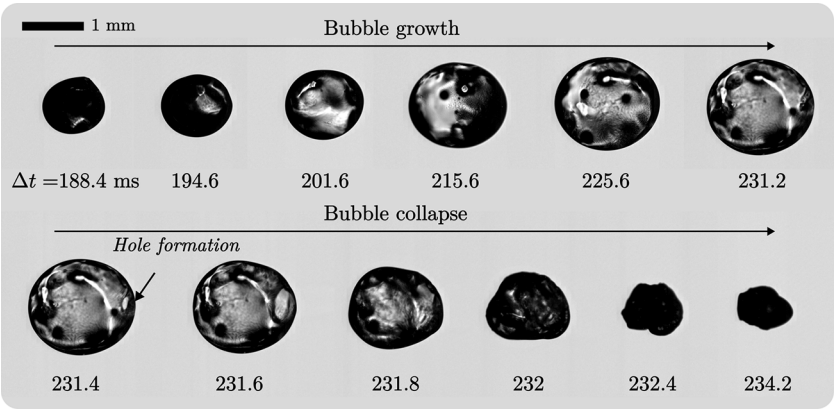

FIG. 18. Sequence of images showing the growth and collapse of a bubble in the late stage, undergoing collapse through hole formation.

The progressive loss of volatile liquid components and the concurrent increase in the relative concentration of the nonvolatile surfactant AOT induce a transition within the droplet material, forming a highly viscous droplet. As a consequence, the vapor bubble growth rate is significantly reduced at this stage, with characteristic growth rates on the order of $\mathcal{O}(10^{-2}$–$10^{-1})$. This reduction reflects the altered rheological behavior of the enriched phase, which suppresses interfacial deformation and inhibits the development of hydrodynamic instabilities on the bubble surface. Collapse of these vapor bubbles is initiated by the formation of a localized rupture in the increasingly viscous interfacial layer, as shown in Fig. 18.

The temporal variation of the bubble size is plotted in Fig. 19. It is observed that the growth rate of the bubble increases with the irradiation intensity. However, the growth rate depends on heating energy and the material properties. It can also be observed from Fig. 19 that the rate of bubble collapse is much faster ($\sim\mathcal{O}(10^0)$) compared to its growth. As previously elucidated, this mode of droplet breakup exhibits a repetitive occurrence. It is observed to repeat 4–10 times for a given trial.

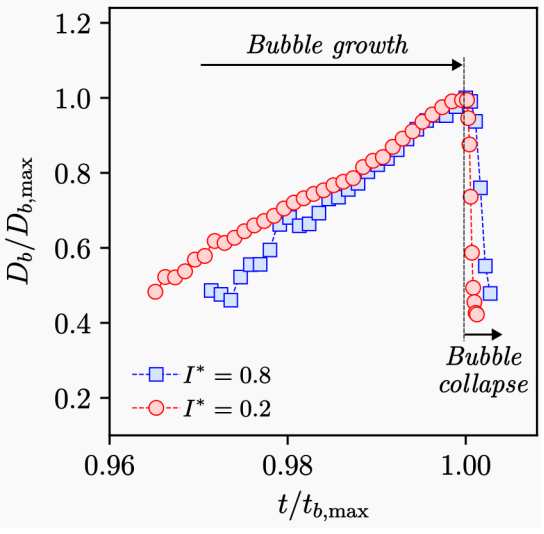

FIG. 19. Temporal evolution of late-stage bubble growth and collapse dynamics, illustrating the variation in bubble size under two different irradiation intensities.

It is pertinent to note that atomization is not observed in this particular mode due to extremely high viscosity of bubble film, which inhibits the growth of instabilities at the bubble interface. It only undergoes shape deformation during bubble collapse due to the propulsive reactionary force induced by the ejection of vapor.

IV. CONCLUSIONS

In this study, we examined the bubble dynamics and breakup behavior of levitated microemulsion droplets during evaporation. The key conclusions drawn from this study are:

(1) The fragmentation behavior of the droplets strongly depends on the heating rate as well as microemulsion composition, leading to three distinct breakup modes (Types A, B, and C), which are further subdivided into several breakup regimes.

(2) A breakup impact parameter (β) is used to characterize the vapor bubble growth and associated instabilities. Two primary bubble rupture mechanisms are identified: (1) Bubble rupture initiated by the growth of Faraday waves on the surface ($\beta \geqslant 1$). (2) A rapidly expanding bubble induces RT waves, destabilizing the bubble film, and ultimately leading to its rupture ($\beta < 1$).

(3) When ($\beta \gg 1$), the bubble rupture leads to the formation of a rim, which, in turn, experiences RT instability, driven by the centripetal acceleration of the retracting fluid. This instability causes the rim to deform into ligaments, breaking into secondary droplets.

(4) The bubble growth and collapse events ($10^{-3} < \beta < 10$) also lead to the ligament-mediated breakup, resulting in the secondary droplets. The ejected ligaments do not always undergo breakup, and only ligaments with a sufficiently large aspect ratio (AR $\geqslant 10$) become unstable and undergo breakup.

(5) For ligaments with an aspect ratio AR > 10, the breakup can be further classified into two types: symmetric and asymmetric. Symmetric breakup is typically associated with higher-momentum ligaments, which involves the destabilization and fragmentation of the entire ligament into multiple droplets. In contrast, the breakup of a low-momentum ligament results in asymmetric breakup, where a single droplet is pinched off from the tip of the ligament.

(6) Xylene microemulsion droplets were observed to exhibit breakup via sheet fragmentation at higher heating rates ($I^* \geqslant 0.4$). This process occurs when a small sized ($\beta \ll 1$) high pressure bubble undergoes breakup, forming a thin liquid sheet. As this sheet retracts, its edge fragments into tiny droplets.

(7) At the end of the droplet lifetime, repetitive cycles of growth and collapse of highly viscous bubbles are observed. The formation and characteristics of this bubble are consistent with progressive surfactant enrichment within the droplet during evaporation, suggesting that surfactant concentration plays a key role in shell evolution.

ACKNOWLEDGMENTS

The authors thank Dr. Gannena K. S. Raghuram for his assistance with the rheology experiments. We also acknowledge the DST–FIST grant at the Department of Chemical Engineering, IIT Madras. Funding support from the SPARC program (Grant ID. 2645) at the Department of Mechanical Engineering, IISc Bengaluru, is gratefully acknowledged.

DATA AVAILABILITY

The data that support the findings of this article are not publicly available upon publication because it is not technically feasible and/or the cost of preparing, depositing, and hosting the data would be prohibitive within the terms of this research project. The data are available from the authors upon reasonable request.

[1] K. Samborska, I. Budziak-Wieczorek, A. Matwijczuk, D. Witrowa-Rajchert, M. Gagoś, B. Gładyszewska, D. Karcz, K. Rybak, M. Jaskulski, A. Barańska, *et al.*, Powdered plant beverages obtained by spray-drying without carrier addition-physicochemical and chemometric studies, Sci. Rep. **14**, 4488 (2024).
[2] B. Krishan, P. Rastogi, D. C. K. Rao, N. S. Kaisare, M. G. Basavaraj, and S. Basu, Evaporation of stable microemulsion droplets, Phys. Fluids **36**, 107162 (2024).
[3] S. Priyadarshini, A. Yadav, A. Kushari, and D. C. K. Rao, Controlling the atomization of burning emulsion droplets, Int. J. Multiphase Flow **193**, 105418 (2025).
[4] K. Pandey, K. Chattopadhyay, and S. Basu, Combustion dynamics of low vapour pressure nanofuel droplets, Phys. Fluids **29**, 074102 (2017).
[5] D. C. K. Rao, S. Karmakar, and S. Basu, Atomization characteristics and instabilities in the combustion of multi-component fuel droplets with high volatility differential, Sci. Rep. **7**, 8925 (2017).
[6] D. Rao, S. Karmakar, and S. Basu, Bubble dynamics and atomization mechanisms in burning multi-component droplets, Phys. Fluids **30**, 067101 (2018).
[7] H. S. Dhami, P. R. Panda, and K. Viswanathan, Production of powders for metal additive manufacturing applications using surface grinding, Manufacturing Letters **32**, 54 (2022).
[8] S. Sharma, N. K. Chandra, A. Kumar, and S. Basu, Shock-induced atomisation of a liquid metal droplet, J. Fluid Mech. **972**, A7 (2023).
[9] D. Guildenbecher, C. López-Rivera, and P. Sojka, Secondary atomization, Exp. Fluids **46**, 371 (2009).
[10] K. Pandey and S. Basu, How boiling happens in nanofuel droplets, Phys. Fluids **30**, 107103 (2018).
[11] K. Pandey, S. Basu, B. Krishan, *et al.*, Dynamic self-tuning, flickering and shedding in buoyant droplet diffusion flames under acoustic excitation, Proc. Combust. Inst. **38**, 3141 (2021).
[12] G. Vadlamudi, B. Krishan, A. Choudhary, and S. Basu, Effect of transient shell formation on shock-induced atomization of an evaporating nanofluid droplet, arXiv:2508.14733.
[13] J. Eggers and E. Villermaux, Physics of liquid jets, Rep. Prog. Phys. **71**, 036601 (2008).
[14] I. M. Jackiw and N. Ashgriz, On aerodynamic droplet breakup, J. Fluid Mech. **913**, A33 (2021).
[15] N. K. Chandra, S. Sharma, S. Basu, and A. Kumar, Aerodynamic bag breakup of a polymeric droplet, Phys. Rev. Fluids **9**, 113303 (2024).
[16] K. Mahesh, The interaction of jets with crossflow, Annu. Rev. Fluid Mech. **45**, 379 (2013).
[17] A. R. Karagozian, The jet in crossflow, Phys. Fluids **26**, 101303 (2014).
[18] J. Andreopoulos, On the structure of jets in a crossflow, J. Fluid Mech. **157**, 163 (1985).
[19] S. Sharma, A. P. Singh, S. S. Rao, A. Kumar, and S. Basu, Shock induced aerobreakup of a droplet, J. Fluid Mech. **929**, A27 (2021).
[20] S. J. Rao and S. Basu, Secondary atomization of droplets at extreme conditions, Annu. Rev. Fluid Mech. **58**, 83 (2025).
[21] D. C. Blanchard, The electrification of the atmosphere by particles from bubbles in the sea, Prog. Oceanogr. **1**, 73 (1963).
[22] L. Deike, E. Ghabache, G. Liger-Belair, A. K. Das, S. Zaleski, S. Popinet, and T. Séon, Dynamics of jets produced by bursting bubbles, Phys. Rev. Fluids **3**, 013603 (2018).
[23] D. C. K. Rao and S. Basu, Atomization modes for levitating emulsified droplets undergoing phase change, Exp. Fluids **61**, 41 (2020).
[24] C. Inoue, Y. I. Izato, A. Miyake, and E. Villermaux, Direct self-sustained fragmentation cascade of reactive droplets, Phys. Rev. Lett. **118**, 074502 (2017).
[25] S.-P. Lin, *Breakup of Liquid Sheets and Jets* (Cambridge University Press, Cambridge, UK, 2003).
[26] A. H. Lefebvre and V. G. McDonell, *Atomization and Sprays* (CRC Press, Boca Raton, FL, 2017).
[27] P. Rastogi, N. S. Kaisare, and M. G. Basavaraj, Diesel emulsion fuels with ultralong stability, Energy Fuels **33**, 12227 (2019).
[28] A. Miglani, S. Basu, and R. Kumar, Insight into instabilities in burning droplets, Phys. Fluids **26**, 032101 (2014).
[29] S. Basu and A. Miglani, Combustion and heat transfer characteristics of nanofluid fuel droplets: A short review, Int. J. Heat Mass Transf. **96**, 482 (2016).
[30] P. Rastogi, N. S. Kaisare, and M. G. Basavaraj, Emulsions as viable alternative to conventional fuels: Current status and challenges, Langmuir **40**, 2800 (2024).

[31] T. Kadota and H. Yamasaki, Recent advances in the combustion of water fuel emulsion, Prog. Energy Combust. Sci. **28**, 385 (2002).
[32] D. Chaitanya Kumar Rao and S. Basu, Phenomenology of disruptive breakup mechanism of a levitated evaporating emulsion droplet, Exp. Therm Fluid Sci. **115**, 110086 (2020).
[33] K. S. R. Gannena, D. C. K. Rao, D. Roy, A. Kumar, and S. Basu, Bubble dynamics and atomization in evaporating polymeric droplets, J. Fluid Mech. **951**, A48 (2022).
[34] S. Priyadarshini, A. Kushari, and D. C. K. Rao, Atomization behavior of burning stable emulsion droplets, Fuel **371**, 131989 (2024).
[35] J. Shinjo, J. Xia, L. Ganippa, and A. Megaritis, Physics of puffing and microexplosion of emulsion fuel droplets, Phys. Fluids **26**, 103302 (2014).
[36] C. Law, C. Lee, and N. Srinivasan, Combustion characteristics of water-in-oil emulsion droplets, Combust. Flame **37**, 125 (1980).
[37] J. Lasheras, A. Fernandez-Pello, and F. Dryer, Initial observations on the free droplet combustion characteristics of water-in-fuel emulsions, Combust. Sci. Technol. **21**, 1 (1979).
[38] G. Jackson and C. Avedisian, Combustion of unsupported water-in-n-heptane emulsion droplets in a convection-free environment, Int. J. Heat Mass Transf. **41**, 2503 (1998).
[39] P. K. Kirar, N. Kumar, and K. C. Sahu, Dynamics of jet breakup and the resultant drop size distribution-effect of nozzle size and impingement velocity, Phys. Fluids **36**, 102108 (2024).
[40] M. Domschke, M. Kraska, R. Feile, and B. Stühn, AOT microemulsions: Droplet size and clustering in the temperature range between the supercooled state and the upper phase boundary, Soft Matter **9**, 11503 (2013).
[41] K. Aoki and K. Hasegawa, Acoustically induced breakup of levitated droplets, AIP Adv. **10**, 055115 (2020).
[42] M. Naka and K. Hasegawa, Breakup characteristics of levitated droplets in a resonant acoustic field, Phys. Fluids **32**, 124109 (2020).
[43] E. Cancino-Jaque, J. Meneses-Diaz, Y. Vargas-Hernández, and L. Gaete-Garretón, On the dynamics of a big drop in acoustic levitation, Ultrason. Sonochem. **101**, 106705 (2023).
[44] S. K. Saroj and R. M. Thaokar, Atomisation of an acoustically levitated droplet: Experimental observations of myriad complex phenomena, J. Fluid Mech. **999**, A89 (2024).
[45] See Supplemental Material at http://link.aps.org/supplemental/10.1103/prbb-cbyr for additional information.
[46] B.-S. Park and R. L. Armstrong, Laser droplet heating: Fast and slow heating regimes, Appl. Opt. **28**, 3671 (1989).
[47] M. Mikami, T. Yagi, and N. Kojima, Occurrence probability of microexplosion in droplet combustion of miscible binary fuels, in *Proceedings of the International Symposium on Combustion* (Elsevier, Amsterdam, 1998), Vol. 27, pp. 1933–1941.
[48] M. Mikami and N. Kojima, An experimental and modeling study on stochastic aspects of microexplosion of binary-fuel droplets, Proc. Combust. Inst. **29**, 551 (2002).
[49] D. C. K. Rao, S. Karmakar, and S. Som, Puffing and micro-explosion behavior in combustion of butanol/Jet A-1 and acetone-butanol-ethanol (ABE)/Jet A-1 fuel droplets, Combust. Sci. Technol. **189**, 1796 (2017).
[50] G. K. S. Raghuram, D. Roy, D. C. K. Rao, A. Kumar, and S. Basu, Insights into bubble–droplet interactions in high-viscoelastic evaporating polymer droplets, Exp. Fluids **65**, 105 (2024).
[51] A. Saha, S. Basu, and R. Kumar, Velocity and rotation measurements in acoustically levitated droplets, Phys. Lett. A **376**, 3185 (2012).
[52] K. Hasegawa, Y. Abe, and A. Goda, Microlayered flow structure around an acoustically levitated droplet under a phase-change process, npj Microgravity **2**, 16004 (2016).
[53] S. Basu, E. Tijerino, and R. Kumar, Insight into morphology changes of nanoparticle laden droplets in acoustic field, Appl. Phys. Lett. **102**, 141602 (2013).
[54] A. L. Yarin, G. Brenn, O. Kastner, D. Rensink, and C. Tropea, Evaporation of acoustically levitated droplets, J. Fluid Mech. **399**, 151 (1999).

[55] S. Shen, Z. Che, T. Wang, Z. Yue, K. Sun, and S. Som, A model for droplet heating and evaporation of water-in-oil emulsified fuel, Fuel **266**, 116710 (2020).
[56] R. J. Lang, Ultrasonic atomization of liquids, J. Acoust. Soc. Am. **34**, 6 (1962).
[57] F. E. Culick, Comments on a ruptured soap film, J. Appl. Phys. **31**, 1128 (1960).
[58] H. K. Habibi and R. Krechetnikov, Soap film catastrophes, J. Fluid Mech. **926**, A19 (2021).
[59] J. Bico, Cracks in bursting soap films, J. Fluid Mech. **778**, 1 (2015).
[60] P. C. Petit, M. Le Merrer, and A.-L. Biance, Holes and cracks in rigid foam films, J. Fluid Mech. **774**, R3 (2015).
[61] H. Lhuissier and E. Villermaux, Bursting bubbles, Phys. Fluids **21**, 091111 (2009).
[62] E. Villermaux, X. Wang, and L. Deike, Bubbles spray aerosols: Certitudes and mysteries, PNAS Nexus **1**, pgac261 (2022).
[63] H. Lhuissier and E. Villermaux, Bursting bubble aerosols, J. Fluid Mech. **696**, 5 (2012).
[64] R. Schulkes, The contraction of liquid filaments, J. Fluid Mech. **309**, 277 (1996).
[65] P. K. Notz and O. A. Basaran, Dynamics and breakup of a contracting liquid filament, J. Fluid Mech. **512**, 223 (2004).
[66] A. A. Castrejón-Pita, J. R. Castrejón-Pita, and I. M. Hutchings, Breakup of liquid filaments, Phys. Rev. Lett. **108**, 074506 (2012).